Chapter 12

Homogenized limit analysis of periodic masonry using simplified micromechanical models

G. Milani[1], A. Taliercio[2]

[1]Department of Architecture, Built Environment and Construction Engineering (ABC), Politecnico di Milano, Milan, Italy, [2]Department of Civil and Environmental Engineering (DICA), Politecnico di Milano, Milan, Italy

12.1 INTRODUCTION

Masonry structures are comprised of units (such as bricks and/or stones), more or less regularly spaced, and usually bonded with mortar.

Predicting the global (or macroscopic, or effective) mechanical properties of masonry according to the mechanical and geometrical properties of units and mortar is a goal that many authors have tried to achieve.

Two approaches are mainly used in the literature for the description of the mechanical behavior of masonry, usually known as macro- and micromodeling.

Macromodeling (see, e.g., Berto et al., 2002; Lourenço, 1996, 1997; Lourenço et al., 1997; Pelà et al., 2011, 2013; Ushaksaraei and Pietruszczak, 2002, just to quote a few) does not make any distinction between bricks and joints, and "smears" the effects of mortar through the formulation of a fictitious homogeneous material. The advantage of macromodeling is linked to the ability of analyzing entire buildings using large-size finite elements (FEs), totally disregarding the actual layout of the units. Unfortunately, it usually requires that many mechanical parameters available be available: they can be obtained by best fitting data provided by costly experimental campaigns performed on full-scale masonry specimens, which require cumbersome devices. On the other hand, specimens sufficiently large to be representative of the global behavior of masonry are virtually impossible to extract and submit to laboratory tests, especially in the case of historic buildings. In addition, the

Numerical Modelling of Masonry and Historical Structures, https://doi.org/10.1016/B978-0-08-102439-3.00012-9

analysis of a different masonry material or brick pattern would require a new calibration of the model parameters and hence new experimentations.

The alternative micromodeling approach (see, e.g., de Felice, 2011; de Felice and Giannini, 2001; Gilbert et al., 2006; Lotfi and Shing, 1994; Lourenço and Rots, 1997; Macorini and Izzuddin, 2011; Milani, 2008; Minga et al., 2018a,b; Portioli et al., 2013; Sutcliffe et al., 2001; Shieh-Beygi and Pietruszczak, 2008) is a distinct representation of mortar joints and bricks. The calibration of the mechanical parameters is easier and less expensive, because only laboratory tests on brick and mortar small samples have to be performed. In order to limit the number of degrees of freedom (DOF) in structural analyses, joints are usually reduced to zero-thickness interfaces, but still the numerical effort remains proportional to the number of units in the structure: accordingly, this approach is feasible for small structural elements (e.g., panels or single piers).

Homogenization (see, e.g., Anthoine, 1995, 1997; Casolo and Milani, 2010; Cecchi et al., 2005, 2007; Cecchi and Milani, 2008; Cluni and Gusella, 2004; Dallot et al., 2008; de Buhan and de Felice, 1997; Kawa et al., 2008; Luciano and Sacco, 1997, 1998; Milani, 2009, 2011a,b,c, 2015; Milani et al., 2006a,b,c; Milani and Taliercio, 2015, 2016; Milani and Tralli, 2012; Mistler et al., 2007; Pande et al., 1989; Pegon and Anthoine, 1997; Pietruszczak and Niu, 1992; Sab, 2003; Sab et al., 2007; Sacco, 2009; Stefanou et al., 2015; Taliercio, 2014; Zucchini and Lourenço, 2002, 2007) is an interesting compromise between micro- and macromodeling, because it allows a structure to be roughly discretized, but at the same time accounts for the mechanical behavior at the mesoscale at each Gauss point accurately. The practical advantage of homogenization stands is therefore the fact that only the mechanical parameters of the constituent materials (brick and mortar) are required to estimate the average behavior of masonry to be used in structural analyses. Additionally, in large-scale computations FE meshes unrelated to the brick size can be used.

From a macroscopic point of view, if units are arranged according to a regular pattern, masonry is an orthotropic medium.

The macroscopic behavior of masonry beyond the elasticity limit was mathematically described by Pietruszczak and Niu (1992), assuming bricks to be elastic-brittle and mortar to be elastoplastic and hardening. Their approach allowed macroscopic failure surfaces for different orientations of the principal stresses to the bed joints to be determined. Damage effects in the constituents were taken into account (e.g., by Luciano and Sacco, 1997; Shieh-Beygi and Pietruszczak, 2008; Zucchini and Lourenço, 2007) to describe the brittle post-peak behavior experimentally observed in tests on masonry specimens. More recently, Sacco (2009) predicted the macroscopic behavior of 2D brickwork in the nonlinear range by assuming damage and friction effects to develop only in the mortar joints, and applying classical homogenization techniques for periodic media to any represenvative volume element (RVE). The major limitation of homogenization is related to nonlinear FE computations, because a

continuous interaction between meso- and macroscale is needed beyond the linear range. This issue involves a huge computational effort, since the field problem has to be solved numerically at each loading step and at all Gauss points.

Apart from the prediction of the incremental inelastic response of large-scale masonry structures, from an engineering point of view it is interesting to get direct information on the behavior of masonry at failure (Gilbert et al., 2006; Milani, 2008, 2009, 2011a,b,c). The aim is to provide designers with reliable and efficient tools for fast estimates of the load-carrying capacity and the active failure mechanisms.

In this framework, limit analysis combined with homogenization theory is an interesting technique that straightforwardly predicts the ultimate behavior of entire structures. This approach requires only a reduced number of material parameters to be known, avoids units and joints to be separately modeled, and allows analyses at the meso- and macroscales to be independently performed. In other words, at a first step homogenized failure surfaces for masonry can be estimated at the mesoscale, without nesting the mesoscale into the FE code used at the macroscale. This is a remarkable advantage that has recently allowed a specific research stream to be developed, to derive advanced models for the evaluation of macroscopic strength domains for masonry walls under in- and out-of-plane loads; see, for example, Cecchi et al. (2007), Cecchi and Milani (2008), de Buhan and de Felice (1997), Luciano and Sacco (1997), Milani (2009, 2011a,b,c), Milani et al. (2006a,b), Milani and Taliercio (2015, 2016), Milani and Tralli (2012), Sab (2003), Sab et al. (2007), and Stefanou et al. (2015). The second step is the implementation of these domains at the structural scale, to perform FE limit analyses on entire buildings (see, e.g., Milani et al., 2006b; Milani, 2015): limit load multipliers, failure mechanisms, and stress distributions at collapse, at least at critical sections, can be obtained.

Focusing on the mesoscale, assuming mortar and bricks to be rigid-perfectly plastic with associated flow rule, and within the basic assumptions of homogenization theory for periodic media, macroscopic strength domains for masonry can be estimated using the classic upper and lower bound theorems of limit analysis applied to an elementary cell (Suquet, 1983, 1987). In particular, the lower bound approach requires statically and plastically periodic microstress fields to be considered, and allows lower bound estimates of the actual homogenized failure domain to be obtained by means of the constrained maximization of the macroscopic stresses. Dually, the upper bound approach requires kinematically admissible, that is, strain rate-periodic, velocity fields to be dealt with, and allows the upper bound of the actual homogenized failure domain to be obtained using the constrained minimization of the total internal power dissipation. In both approaches, the mechanical problem is matched by (non)linear mathematical programming problem, where the total number of optimization unknowns is extremely reduced.

This chapter is aimed at critically reviewing some available recent and effective models, with a comparison of their numerical performances. In particular, four different strategies for the evaluation of the homogenized strength domain of running or header bond masonry under in-plane and out-of-plane loads are discussed and critically compared.

Two of these models give lower bounds on the macroscopic strength domain of periodic masonry, and two give upper bounds. The first lower bound model (Milani et al., 2006a,c) subdivides the elementary cell into a few rectangular subdomains, in which the microstress field is expanded using polynomial expressions. In the second lower bound procedure (Milani, 2011a,c), joints are reduced to interfaces and bricks are subdivided into a few constant stress triangular (CST) elements: closed-form estimates of the homogenized strength domain can be determined. The third procedure (Cecchi et al., 2007; Cecchi and Milani, 2008) is a "compatible identification" approach, with joints reduced to interfaces and bricks assumed to be infinitely resistant. The velocity field is assumed to be a linear combination of elementary deformation modes applied to the elementary cell. The last model is a kinematically admissible procedure based on the so-called Method of Cells (MoC; see Milani and Taliercio 2015, 2016), where the elementary cell is subdivided into six rectangular subcells with prescribed polynomial strain rate-periodic velocity fields. The first and latter approaches have the advantage that the finite thickness of the joints is explicitly taken into account. In the second approach, although joints are reduced to interfaces with frictional behavior, failure inside bricks can be accounted for. The third approach is the most straightforward, but is reliable only in the case of thin joints and strong blocks. A critical comparison of the pros and cons of all models is discussed, with reference to some examples of engineering interest.

12.2 FUNDAMENTALS OF HOMOGENIZATION FOR PERIODIC MEDIA

When heterogeneous media are dealt with, it is customary to replace the real medium Ω by a "homogenized" one and define its global (or macroscopic) properties through the analysis of a RVE. The RVE is the smallest part of the real medium that contains all the information required to completely characterize its average mechanical behavior. If the medium is periodic a single "unit cell" (Y) can be used as RVE. Y^m and Y^b will denote the parts of the cell occupied by mortar and brick, respectively.

Masonry is a composite material, usually made of units bonded with mortar joints; in several instances, units and mortar are periodically arranged. Due to its periodicity, an entire masonry wall Ω can be seen as the spatial repetition of unit cells (see Fig. 12.1). If a running- or header-bond bond pattern is considered, a possible choice for the unit cell is a rectangle, as shown in Fig. 12.1.

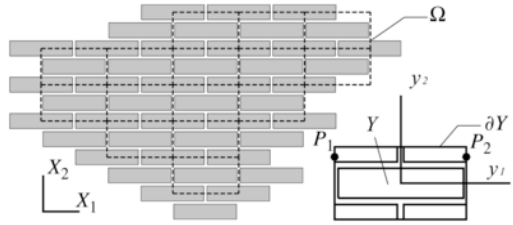

FIGURE 12.1 Typical running bond assemblage of bricks and mortar and possible unit cell.

For periodic arrangements of units and mortar, homogenization techniques can be used both in the elastic and inelastic range, taking into account the microstructure only at a cell level. This leads to a significant simplification in the numerical models adopted for studying entire walls, especially for the inelastic case.

The basic idea of any homogenization procedure consists in defining macroscopic stresses and strains (denoted by $\mathbf{E}$ and $\mathbf{\Sigma}$, respectively) that represent the corresponding microscopic quantities $\boldsymbol{\sigma}$ and $\boldsymbol{\varepsilon}$ averaged over the cell:

$$\begin{aligned} \mathbf{E} &= \langle \boldsymbol{\varepsilon} \rangle = \frac{1}{A}\int_Y \boldsymbol{\varepsilon}(\mathbf{u}) dY \\ \mathbf{\Sigma} &= \langle \boldsymbol{\sigma} \rangle = \frac{1}{A}\int_Y \boldsymbol{\sigma} dY \end{aligned} \tag{12.1}$$

where A is the area of the elementary (2D) cell, $\mathbf{u}$ is the microscopic displacement field, and $\langle * \rangle$ is the averaging operator.

Suitable periodicity conditions are imposed on $\boldsymbol{\sigma}$ and $\mathbf{u}$, that is:

$$\begin{cases} \mathbf{u} = \mathbf{E}\mathbf{y} + \mathbf{u}^{\text{per}} & \mathbf{u}^{\text{per}} \text{ on } \partial Y \\ \boldsymbol{\sigma}\mathbf{n} & \text{anti} - \text{periodic on } \partial Y \end{cases} \tag{12.2}$$

where $\mathbf{u}^{\text{per}}$ is the periodic part of $\mathbf{u}$ and ∂Y is the boundary of Y.

Assume both materials to be rigid-perfectly plastic and to obey an associated flow rule. Let S^m, S^b, and S^{hom} denote the strength domains of mortar, units, and homogenized material, respectively. It was proved by Suquet (1983) that the static definition of S^{hom} in the space of the macroscopic stresses reads:

$$S^{\text{hom}} = \left\{ \sum : \left\{ \begin{array}{rll} \sum = \langle \boldsymbol{\sigma} \rangle = \frac{1}{A}\int_Y \boldsymbol{\sigma} dY & & \text{(a)} \\ div\, \boldsymbol{\sigma} = \mathbf{0} & & \text{(b)} \\ [[\boldsymbol{\sigma}]]\, \mathbf{n}^{\text{int}} = \mathbf{0} \quad \text{on} \quad S_\sigma & & \text{(c)} \\ \boldsymbol{\sigma}\mathbf{n} \quad \text{anti} - \text{periodic} \quad \text{on} \quad \partial Y & & \text{(d)} \\ \boldsymbol{\sigma}(\mathbf{y}) \in S^m \quad \forall \mathbf{y} \in Y^m; & \boldsymbol{\sigma}(\mathbf{y}) \in S^b \quad \forall \mathbf{y} \in Y^b & \text{(e)} \end{array} \right\} \right. \tag{12}$$

where $[[\boldsymbol{\sigma}]]$ is the jump in microstresses across any discontinuity surface S_σ

and $\mathbf{n}^{\text{int}}$ is the normal to S_σ at any point. Condition (12.3b) imposes the microequilibrium, condition (12.3d) derives from periodicity, and condition (12.3e) represents the yield criteria for the components (brick and mortar).

Any point of the homogenized failure surface can be determined by prescribing a direction in the homogenized stress space by means of a unit vector $\mathbf{n}_\Sigma$ and solving the following constrained maximization problem:

$$\text{Find } \max\{\lambda\} : \begin{cases} \lambda \mathbf{n}_\Sigma = \frac{1}{Y}\int_Y \boldsymbol{\sigma} dY \\ \boldsymbol{\sigma}\mathbf{n} \quad \text{anti}-\text{periodic} \quad \text{on} \quad \partial Y \\ div\boldsymbol{\sigma} = \mathbf{0} \\ \boldsymbol{\sigma}(\mathbf{y}) \in S^i(\mathbf{y}) = \begin{cases} S^b & \text{if } y \in Y^b \\ S^m & \text{if } y \in Y^m \end{cases} \end{cases} \tag{12.4}$$

where $\lambda \mathbf{n}_\Sigma$ is a macroscopic stress on the boundary of S^{hom} belonging to a straight line, oriented as $\mathbf{n}_\Sigma$. If masonry is assumed to be in a state of plane stress in the plane (x_1, x_2), $\mathbf{n}_\Sigma = \begin{bmatrix} \alpha & \beta & \gamma \end{bmatrix}^T$ is a unit vector in the macroscopic stress space (Σ_{11}, Σ_{22}, Σ_{12}); see Fig. 12.2A.

A dual kinematic definition of S^{hom}, also due to Suquet (1983), can be derived through its support function $\pi^{\text{hom}}(\mathbf{D})$ as follows:

$$S^{\text{hom}} = \left\{ \boldsymbol{\Sigma} : \begin{cases} \boldsymbol{\Sigma} : \mathbf{D} \le \pi^{\text{hom}}(\mathbf{D}) \quad \forall \mathbf{D} \in R^6 \\ \pi^{\text{hom}}(\mathbf{D}) = \inf_{\mathbf{v}} \left\{ P(\mathbf{v}) : \left| \mathbf{D} = \frac{1}{Y}\int_{\partial Y} \mathbf{v} \overset{s}{\otimes} \mathbf{n} dS \right. \right\} \\ P(\mathbf{v}) = \int_Y \pi(\mathbf{d}) dY + \int_S \pi([[\mathbf{v}]]; \mathbf{n}_v) dS \end{cases} \right\} \tag{12.}$$

where $\mathbf{v} = \mathbf{D}\mathbf{y} + \mathbf{v}^{\text{per}}$ is the microscopic velocity field, and $\mathbf{v}^{\text{per}}$ is its periodic part; $\mathbf{d}$ and $\mathbf{D}$ are the microscopic and macroscopic strain rates, respectively; S is any discontinuity surface for $\mathbf{v}$ in Y, and $\mathbf{n}_v$ is the normal to S; $\overset{s}{\otimes}$ denotes the

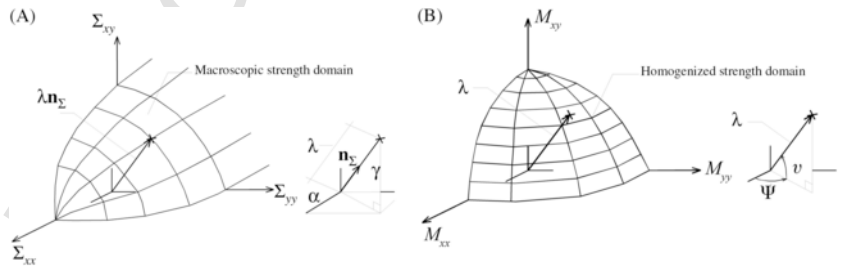

FIGURE 12.2 (A) In-plane homogenization problem. Meaning of the multiplier λ in the homogenized stress space ($\Sigma_{11}=\Sigma_{xx}=\alpha$, $\Sigma_{22}=\Sigma_{yy}=\beta$ and $\Sigma_{12}=\Sigma_{xy}=\gamma$). (B) Out-of-plane homogenization problem. Meaning of the multiplier λ in the optimization problem and angles Ψ and ϑ.

symmetric part of the dyadic product of two vectors; $\pi(\mathbf{d}) = \max_{\boldsymbol{\sigma}} \{\boldsymbol{\sigma} : \mathbf{d};\ \ \boldsymbol{\sigma} \in S(\mathbf{y})\}$; $\pi([[\mathbf{v}]]; \mathbf{n}_v) = \pi([[\mathbf{v}]] \overset{s}{\otimes} \mathbf{n}_v)$.

12.3 PES MODEL: POLYNOMIAL EXPANSION OF THE MICROSTRESS FIELD

12.3.1 Homogenized yield surface under in-plane loads

The first micromechanical model presented in this chapter for the limit analysis of masonry walls under in- and out-of-plane loads was proposed by Milani et al. (2006a). The model requires a subdivision of the unit cell into 36 subdomains, as shown in Fig. 12.3, in which polynomial microstress fields are defined. Equilibrium inside each subdomain and at the interface between contiguous subdomains is prescribed, together with antiperiodicity conditions for the microscopic stress vector along the boundary of the unit cell.

In each subdomain Y^k, any stress component $\sigma_{ij}^{(k)}$ is expressed as a polynomial of degree m and can be written as follows:

$$\sigma_{ij}^{(k)} = \mathbf{X}(\mathbf{y})\mathbf{S}_{ij}^{T} \quad \mathbf{y} \in Y^k \tag{12.6}$$

where $\mathbf{X}(\mathbf{y}) = \begin{bmatrix} 1 & y_1 & y_2 & y_1^2 & y_1 y_2 & y_2^2 & \dots \end{bmatrix}$, and $\mathbf{S}_{ij} = \begin{bmatrix} S_{ij}^{(1)} & S_{ij}^{(2)} & S_{ij}^{(3)} & S_{ij}^{(4)} & S_{ij}^{(5)} & S_{ij}^{(6)} & \dots \end{bmatrix}$ is an array of $\widetilde{N} = (m+1)(m+2)/2$ entries, representing the unknown stress parameters.

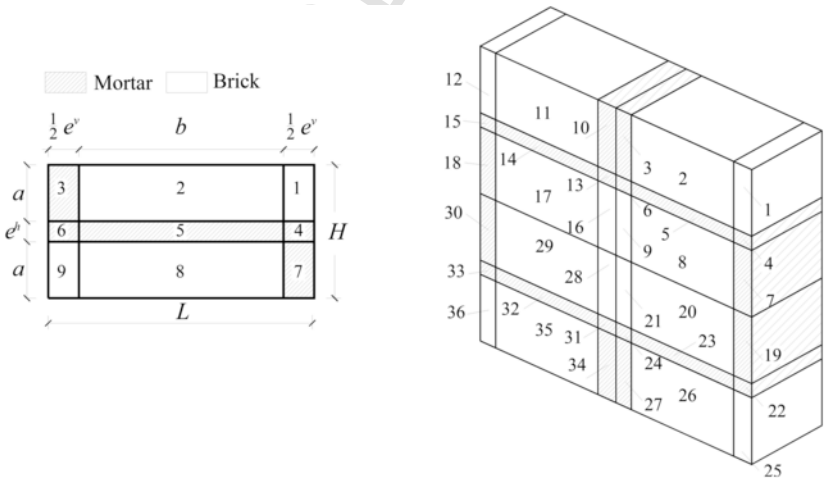

FIGURE 12.3 Subdivision of the unit cell. Left: subdivision and geometrical characteristics of one-fourth of the cell. Right: subdivision of the entire cell into 36 subdomains.

Prescribing equilibrium with zero body forces within every subdomain, continuity of the stress vector at any interface, and antiperiodicity of $\boldsymbol{\sigma}\mathbf{n}$ strongly reduces the total number of independent stress parameters.

In detail, equilibrium within each subdomain reads $\sigma_{ij,j}^{(k)}(y_1, y_2) = 0$, $i = 1, 2$, $\forall (y_1, y_2) \in Y^k$. Since $\sigma_{ij}^{(k)}$ is a polynomial expression of degree (m), any linear combination of its derivatives $(div\boldsymbol{\sigma}^{(k)})$ is a polynomial of degree $(m-1)$. This gives $2N$ linear independent equations in the stress coefficients, where

$$N = ((m-1)^2/2) + (3(m-1)/2) + 1 = (m(m+1)/2)$$

Continuity of the stress vector across any internal interface between two contiguous subdomains (Y^k, Y^r) sharing a common interface of normal $\mathbf{n}$ reads $\sigma_{ij}^{(k)} n_j - \sigma_{ij}^{(r)} n_j = 0$, $i = 1, 2$, $\forall Y^k, Y^r$ (see Fig. 12.4A). The stress component polynomial expressions of degree m along the interface, other $2N'$ additional equations, with $N' = m + 1$, are obtained (see Fig. 12.4B).

Antiperiodicity of $\boldsymbol{\sigma}\mathbf{n}$ on ∂Y gives $2N'$ additional equations per each pair of external faces (m, n) (Fig. 12.5C), where the outward unit normal vectors ($\boldsymbol{n}_1$, $\boldsymbol{n}_2$) are opposite.

Finally, some automatically performed elementary assemblage operations on the local variables allow the stress vector within every subdomain to be expressed as follows:

$$\widetilde{\boldsymbol{\sigma}}^{(k)} = \widetilde{\mathbf{X}}^{(k)}(\mathbf{y})\widetilde{\mathbf{S}} \quad k = 1, \ldots, k^{\max} \tag{12.7}$$

where $\widetilde{\boldsymbol{\sigma}}^{(k)}$ is the array of the in-plane stresses within the k-th subdomain; $\widetilde{\mathbf{S}}$ is the array gathering the N_{un} independent unknown stress parameters; $\widetilde{\mathbf{X}}^{(k)}(\mathbf{y})$ is a $3 \times N_{un}$ matrix that contains only geometrical coefficients; its elements are polynomial forms in the microscopic coordinate $\mathbf{y}$.

The approximated stress field defined in Eq. (12.7) is a statically admissible stress field, so that the constrained maximization problem (12.4) that de-

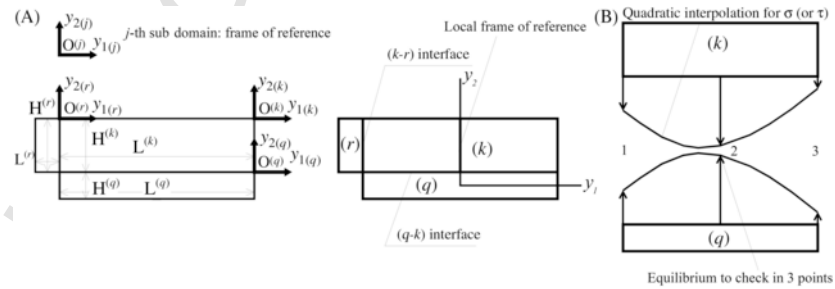

FIGURE 12.4 Contiguous subdomains. (A) Geometry and reference system for each subdomains and interfaces between adjacent subdomains. (B) Example of equilibrium conditions along a horizontal interface for the normal stress and quadratic expansion of the microstress field.

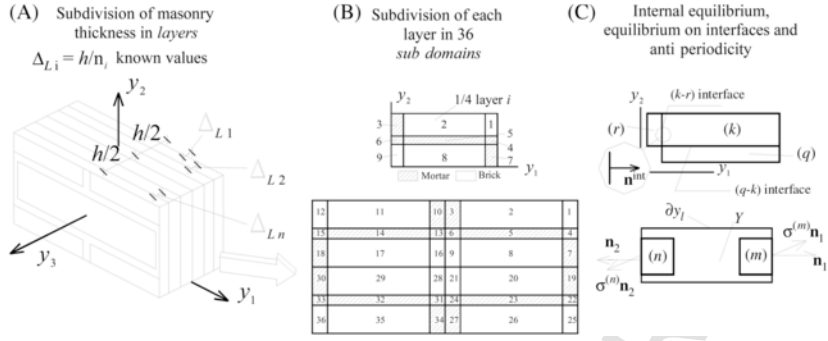

FIGURE 12.5 Micromechanical model proposed for transverse loads. (A) Subdivision of the unit cell into layers along the thickness. (B) Subdivision of each layer into subdomains. (C) Enforcement of equilibrium and periodicity conditions.

fines the macroscopic yield surface in plane stress conditions point by point can be further specialized as follows:

$$\begin{cases} \max\{\lambda\} \\ \text{such that} \begin{cases} \lambda \mathbf{n}_\Sigma = \frac{1}{Y}\sum_{k=1}^{4k^{\max}} \int_Y \widetilde{\mathbf{X}}^{(k)}(\mathbf{y})\widetilde{\mathbf{S}}dY & \text{(a)} \\ \mathbf{y} \in Y & \text{(b)} \\ \widetilde{\boldsymbol{\sigma}} = \widetilde{\mathbf{X}}^{(k)}(\mathbf{y})\widetilde{\mathbf{S}} & \text{(c)} \\ \widetilde{\boldsymbol{\sigma}}(\mathbf{y}) \in S^k \quad k = 1, \ldots, 4k^{\max} & \text{(d)} \end{cases} \end{cases} \tag{12.8}$$

where S^k stands for the failure domain of the component (unit or mortar) belonging to the ith subdomain.

The optimization problem given by Eq. (12.8) is generally nonlinear as a consequence of the (possible) nonlinearity of the yield surfaces of the components. In addition, condition (12.8d) has to be checked at every point of the domain Y. Nevertheless, a continuous check is avoided using classic collocation, that is, imposing plastic admissibility only where the stress is higher. This procedure provides a rigorous lower bound only for polynomial models of order 0 and 1; in all other cases, collocation consists in enforcing, in every subdomain, the admissibility condition on a regular grid of $r \times q$ "nodal points."

Adopting a regular grid, the optimization problem takes the following discretized form:

$$\left\{\begin{array}{l}\max\{\lambda\}\\ \text{such that}\left\{\begin{array}{c}\lambda\mathbf{n}_\Sigma=\frac{1}{Y}\sum_k\int_Y\widetilde{\mathbf{X}}^{(k)}(\mathbf{y})\widetilde{\mathbf{S}}dY\\ \mathbf{y}^j\equiv\text{nodal point}\\ \widetilde{\boldsymbol{\sigma}}^j=\widetilde{\mathbf{X}}^{(k)}(\mathbf{y}^j)\widetilde{\mathbf{S}}\\ \widetilde{\boldsymbol{\sigma}}^j\in S^i\quad j=1,...,rq\\ k=1,...,4k^{\max}\end{array}\right.\end{array}\right. \tag{12.9}$$

Standard linearization of the yield surfaces of brick and mortar allows the problem to be solved by linear programming.

Sections of the in-plane failure surface of masonry can be represented at different angles, ϑ, between a bed joint and the macroscopic horizontal stress (Σ_{11}). By keeping ϑ fixed and varying the angle $\psi=\tan^{-1}\Sigma_{22}/\Sigma_{11}$, where Σ_{22} is the macroscopic vertical stress, any section is drawn. Accordingly, the director cosines of vector $\mathbf{n}_\Sigma$ can be expressed as:

$$\begin{aligned}\mathbf{n}_{\Sigma,1}&=\tfrac{1}{2}(\cos\psi(1+\cos(2\vartheta))+\sin\psi(1-\cos(2\vartheta)))\\ \mathbf{n}_{\Sigma,2}&=\tfrac{1}{2}(\cos\psi(1-\cos(2\vartheta))+\sin\psi(1+\cos(2\vartheta)))\\ \mathbf{n}_{\Sigma,3}&=\tfrac{1}{2}(\cos\psi-\sin\psi)\sin(2\vartheta)\end{aligned} \tag{12.10}$$

The numerical failure surfaces can be therefore obtained by solving the optimization problem given by Eq. (12.4), where the direction of the "load" $\left[\Sigma_{11}\quad\Sigma_{22}\quad\Sigma_{12}\right]^T$ depends on the orientation ϑ of the principal stresses to the joints.

12.3.2 Extension to transverse loads

In order to account for loads acting transversely to a wall, within the framework of the previous discretization into subdomains and polynomial expansions of the stress field, the unit cell is subdivided into a fixed number of layers along its thickness, as shown in Fig. 12.5A. In other words, the out-of-plane model requires a subdivision of the wall into n_L layers of equal thickness $\Delta_L=t/n_L$ (Fig. 12.5A). According to classical limit analysis for thin plates, the out-of-plane components σ_{i3} (i=1,2,3) of the microstress tensor $\boldsymbol{\sigma}$ vanish, so that each layer is subjected only to in-plane stresses σ_{ij} with i,j=1,2. These stresses are assumed to be uniform along the thickness of each layer, that is, in each layer $\sigma_{ij}=\sigma_{ij}(y_1,y_2)$ is a polynomial expansion in the in-plane geometric variables (see Milani et al., 2006a,c and Fig. 12.5B).

Under the same hypotheses done for in-plane loads, any point belonging to the boundary of the homogenized flexural strength domain can be evaluated by solving the following (non)linear optimization problem:

$$\begin{cases} \max\{\lambda\} \\ \text{such that} \begin{cases} \mathbf{N} = \int_{k,i_L} \widetilde{\boldsymbol{\sigma}}^{(k,i_L)} dY dy_3 \\ \mathbf{M} = \int_{k,i_L} y_3 \widetilde{\boldsymbol{\sigma}}^{(k,i_L)} dY dy_3 \\ \mathbf{M} = \begin{bmatrix} M_{11} & M_{12} \\ M_{12} & M_{22} \end{bmatrix} = \lambda \begin{bmatrix} \cos(\psi)\cos(\vartheta) & \sin(\vartheta) \\ \sin(\vartheta) & \sin(\psi)\cos(\vartheta) \end{bmatrix} \\ \psi = [0;\ 2\pi] \quad \theta = [0;\ \pi/2] \\ \widetilde{\boldsymbol{\sigma}}^{(k,i_L)} = \widetilde{\mathbf{X}}^{(k,i_L)}(\mathbf{y})\widetilde{\mathbf{S}} \\ \widetilde{\boldsymbol{\sigma}}^{(k,i_L)} \in S^{(k,i_L)} \\ k = 1, \ldots, \text{ number of sub} - \text{domains}; \ \ i_L = 1, \ldots, \text{number of lay} \end{cases} \end{cases}$$

where λ is the load multiplier along any radial path in the space of the bending and twisting moments (M_{11}, M_{22}, M_{12}; see Fig. 12.2B); ψ and ϑ are spherical coordinates in the space (M_{11}, M_{22}, M_{12}), given by $\tan\ \vartheta = M_{12}/\sqrt{M_{11}^2 + M_{22}^2}$, $\tan\ \psi = M_{22}/M_{11}$; $S^{(k,i_L)}$ denotes the (nonlinear) strength domain of the constituent material (mortar or brick) corresponding to the k^{th} subdomain and i_L^{th} layer; $\widetilde{\mathbf{S}}$ collects all the unknown polynomial coefficients (of all subdomains, of all layers).

It is worth noting that:

- For the sake of simplicity, membrane actions are assumed to be constant and independent from the load multiplier. Hence, in estimating the load-bearing capacity of transversely loaded walls, in-plane actions are only assumed to modify the flexural strength domain of masonry. This assumption is rigorous for laboratory wallettes, where a fixed in-plane vertical compressive load is always applied before any out-of-plane actions, which is then increased to failure. It also acceptable in the analysis of real buildings, which always withstand vertical, in-plane dead loads.
- Condition (f) should be checked at every point of the domain Y, but this is impossible for polynomial expansions of degree higher than 1. The approach used is thus based on collocation, that is, admissibility is checked on a regular grid of "nodal points."
- Similar to the in-plane case, the nonlinearity in the terms $\widetilde{\boldsymbol{\sigma}}^{(k,i_L)} \in S^{(k,i_L)}$, due to the (possible) nonlinearity of the strength domains of the components, can be avoided by a classical piecewise linearization of the domains.

12.4 EQUILIBRATED MODEL WITH JOINTS REDUCED TO INTERFACES AND CONSTANT STRESS TRIANGULAR DISCRETIZATION OF THE BRICKS

12.4.1 Homogenized yield surface under in-plane loads

The second homogenization model presented is also based on a static lower bound approach, in which the unit cell is roughly discretized into FEs, as depicted in Fig. 12.6.

Unlike the previous model, joints are reduced to interfaces of vanishing thickness, and units are discretized using a coarse mesh of three-node plane–stress elements (CST), as schematically sketched in Fig. 12.6. The choice of meshing 1/4 of the brick through at least three triangular elements is due to the need of capturing the presence of shear stresses in the bed joint under horizontal stretching (element 2 in Fig. 12.6). The interfaces within the bricks allow, in principle, failure of the units to be captured.

Here, 24 CST elements are used for the discretization of the unit cell (Fig. 12.6). The superscript (n) denotes any stress component belonging to the n-th element. Assuming plane–stress conditions, the nonvanishing components of the Cauchy stress tensor $\boldsymbol{\sigma}^{(n)}$ within the n-th element are $\sigma_{11}^{(n)}$ (horizontal stress), $\sigma_{22}^{(n)}$ (vertical stress), and $\sigma_{12}^{(n)}$ (shear stress). The total number of un-

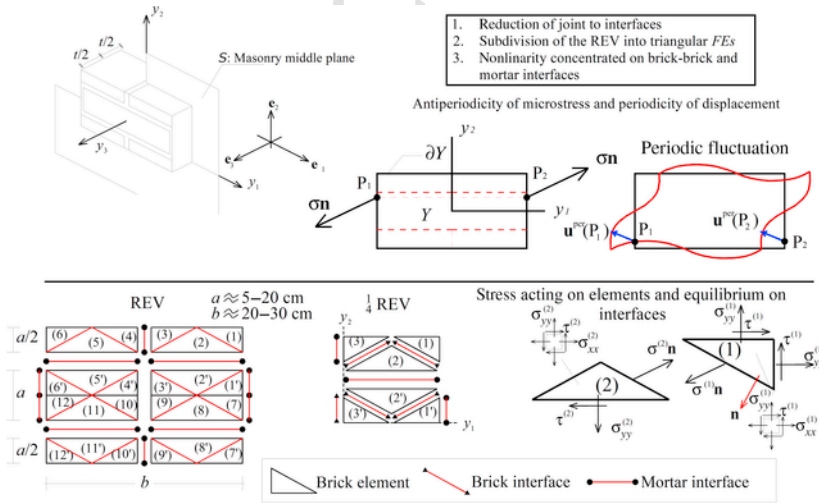

FIGURE 12.6 Lower bound approach with CST discretization of the bricks. Subdivision of the REV into 24 CST triangular elements (and 1/4 into six elements) and antiperiodicity of the microstress field ($\sigma_{xx}^{(n)}=\sigma_{11}^{(n)}$, $\sigma_{yy}^{(n)}=\sigma_{22}^{(n)}$, $\tau^{(n)}=\sigma_{12}^{(n)}$).

knowns is 73, that is, 72 stress components (three per element), and the load multiplier λ.

Equilibrium within each element ($div\boldsymbol{\sigma} = 0$) is a priori fulfilled, because CSTs are used. On the contrary, two equality constraints must be imposed for each internal interface, to ensure continuity of the normal and tangential components of the stress vector across the interface between contiguous elements.

Antiperiodicity constraints for the stress vector are written for the pairs of triangles 1–6, 1′–6′, 7–12, 7′–12′, 1–7′, 3–9′, 4–10′, and 6–12′. For instance, for the pairs 1–6 and 1–7′, the following equality constraints must be prescribed:

$$\left.\begin{aligned}\sigma_{1i}^{(1)} &= \sigma_{1i}^{(6)}\\ \sigma_{2i}^{(1)} &= \sigma_{2i}^{(7\prime)}\end{aligned}\right\} \quad i = 1,2 \tag{12.12}$$

Assuming the strength of both the interfaces and the triangular elements to be limited, the in-plane homogenization problem can be rewritten as follows:

$$\begin{aligned}&\max\{\lambda\}\\ &\text{subject to}\begin{cases}\lambda\alpha = \dfrac{\sum_{i=1}^{24}\sigma_{11}^{(i)}A_i}{2ab}\\ \lambda\beta = \dfrac{\sum_{i=1}^{24}\sigma_{22}^{(i)}A_i}{2ab}\\ \lambda\gamma = \dfrac{\sum_{i=1}^{24}\sigma_{12}^{(i)}A_i}{2ab}\\ \mathbf{A}_{eq}^{I}\mathbf{X} = \mathbf{b}_{eq}^{I}\\ \mathbf{A}_{eq}^{ap}\mathbf{X} = \mathbf{b}_{eq}^{ap}\\ f_E^{\prime}(\sigma_{11}^{(i)},\sigma_{22}^{(i)},\sigma_{12}^{(i)}) \le 0 \quad \forall i = 1,\ldots,24\\ f_I^{\prime}(\sigma_I^{(i)},\tau_I^{(i)}) \le 0 \quad \forall i = 1,\ldots,32\end{cases}\end{aligned} \tag{12.13}$$

The symbols used in Eq. (12.13) have the following meaning:

- α, β, and γ indicate the director cosines of the unit vector $\mathbf{n}_\Sigma$ (see Fig. 12.2,A) in the space of the homogenized membrane stresses. The solution of the optimization problem allows a point on the homogenized failure surface, with coordinates $\Sigma_{11}=\lambda\alpha$, $\Sigma_{22}=\lambda\beta$, and $\Sigma_{12}=\lambda\gamma$, to be determined.
- A_i is the area of the i-th element ($ab/8$ or $ab/16$).
- $\mathbf{X}$ is an array of 73 entries, which collects all the optimization unknowns (elements stress components and collapse multiplier).
- $\mathbf{A}_{eq}^{I}\mathbf{X} = \mathbf{b}_{eq}^{I}$ is a set of linear equations corresponding to equilibrium constraints on all interfaces. Since 32 interfaces are present in the discretized unit cell and two equality constraints have to be fulfilled at each interface, $\mathbf{A}_{eq}^{I}$ is a 64×73 matrix and $\mathbf{b}_{eq}^{I}$ is an array of 64 zero entries.

- $\mathbf{A}_{eq}^{ap}\mathbf{X} = \mathbf{b}_{eq}^{ap}$ collects antiperiodicity conditions, and it is therefore a set of 16 equations. Thus, $\mathbf{A}_{eq}^{ap}$ is a 16×73 matrix, and $\mathbf{b}_{eq}^{ap}$ is an array of 16 zero entries.
- $f_E^i(\sigma_{11}^{(i)}, \sigma_{22}^{(i)}, \sigma_{12}^{(i)}) \leq 0$, i=1,…,24, is a set of nonlinear inequalities defining the strength domain of the i-th element. Within a linear programming scheme, the yield surface is linearized a priori: linearization is usually performed so as to get a safe approximation of the strength domain, to ensure that a strict lower bound estimate of the collapse load is obtained using a static approach. This can be easily obtained using a Delaunay tessellation.
- $f_I^i(\sigma_I^{(i)}, \tau_I^{(i)}) \leq 0$, i=1,…, 32 are inequalities that play the role of $f_E^i \leq 0$ for the interfaces. Two typologies of interfaces are present in the model, namely interfaces within bricks and interfaces corresponding to mortar joints.
- $\sigma_I^{(i)}$ and $\tau_I^{(i)}$ indicate the normal and shear stress acting on interface i, respectively.

Eq. (12.13) is a standard linear programming problem that allows the collapse loads of in-plane loaded masonry structures to be estimated using an FE approach.

12.4.2 Extension to transverse loads

The generalization of the model to out-of-plane actions (under the Kirchhoff–Love hypothesis for thin plates) is performed in the same way followed for the polynomial expansion of the stress field in Par. 3.2, namely with a subdivision of the wall thickness t into n_L layers of equal thickness $\Delta_L = t/n_L$. Within these assumptions, similar to the in-plane case any point of the failure surface in the bending-twisting moment space can be estimated by solving the following linear programming problem:

$$\max\{\lambda\}$$

$$\text{subject to}\begin{cases}\lambda\alpha = \dfrac{\sum_{j=1}^{n_L}{}'_L\left(\frac{t+\Delta_L}{2}-j\Delta_L\right)\sum_{i=1}^{24}\sigma_{11}^{(i,j)}A_i}{2ab}, & N_{11}=\dfrac{\sum_{j=1}^{n_L}\Delta_L\sum_{i=1}^{24}\sigma_{11}^{(i,j)}A_i}{2ab}=\\ \lambda\beta = \dfrac{\sum_{j=1}^{n_L}\Delta_L\left(\frac{t+\Delta_L}{2}-j\Delta_L\right)\sum_{i=1}^{24}\sigma_{22}^{(i,j)}A_i}{2ab}, & N_{22}=\dfrac{\sum_{j=1}^{n_L}\Delta_L\sum_{i=1}^{24}\sigma_{22}^{(i,j)}A_i}{2ab}=\\ \lambda\gamma = \dfrac{\sum_{j=1}^{n_L}\Delta_L\left(\frac{t+\Delta_L}{2}-j\Delta_L\right)\sum_{i=1}^{24}\sigma_{12}^{(i,j)}A_i}{2ab}, & N_{12}=\dfrac{\sum_{j=1}^{n_L}\Delta_L\sum_{i=1}^{24}\sigma_{12}^{(i,j)}A_i}{2ab}=\\ \mathbf{A}_{eq}^{I}\mathbf{X}=\mathbf{b}_{eq}^{I}\\ \mathbf{A}_{eq}^{ap}\mathbf{X}=\mathbf{b}_{eq}^{ap}\\ f_E^{i,j}(\sigma_{11}^{(i,j)},\sigma_{22}^{(i,j)},\sigma_{12}^{(i,j)})\le 0 \quad \forall i=1,\ldots,24,\ \forall j=1,\ldots,n_L\\ f_I^{i,j}(\sigma_I^{(i,j)},\tau_I^{(i,j)})\le 0 \quad \forall i=1,\ldots,32,\ \forall j=1,\ldots,n_L\end{cases}$$

where all the symbols have already been defined in the previous section.

Compared to the in-plane case, the following key issues are worth noting:

- λ is the load multiplier along any radial path in the (M_{11}, M_{22}, M_{12}) space;
- α, β, and γ are the director cosines of the unit vector $\mathbf{n}_\Sigma$ in the (M_{11}, M_{22}, M_{12}) space (see Fig. 12.2B).
- $\mathbf{X}$ is an array that collects all the unknown stresses in all the FEs of all layers. Therefore, $\mathbf{X}$ is an array of $3\times 24\times n_L$ entries.
- $\mathbf{A}_{eq}^{I}\mathbf{X}=\mathbf{b}_{eq}^{I}$ collects equilibrium constraints at the interfaces of all layers. Since no shear stresses are transferred between contiguous layers, for each layer these constraints are the same as in Eq. (12.13). $\mathbf{A}_{eq}^{I}$ is a $64n_L\times(72n_L+1)$ matrix, and $\mathbf{b}_{eq}^{I}$ is an array of $64n_L$ zero entries.
- Similar remarks apply to the set of equations $\mathbf{A}_{eq}^{ap}\mathbf{X}=\mathbf{b}_{eq,}^{ap}$ which collects antiperiodicity and equilibrium conditions for all layers. $\mathbf{A}_{eq}^{ap}$ is now a $16n_L\times(72n_L+1)$ matrix, and $\mathbf{b}_{eq}^{ap}$ is an array of $16n_L$ zero entries.
- Unlike the in-plane case, three additional equality constraints have to be imposed to ensure that the homogenized membrane forces (N_{11}, N_{22}, N_{12}) vanish.

Similar to the procedure followed with the previous lower bound model, membrane actions are kept constant and independent from the load multiplier.

12.5 COMPATIBLE IDENTIFICATION MODEL WITH JOINTS REDUCED TO INTERFACES AND INFINITELY STRONG UNITS

12.5.1 Homogenized yield surface under in-plane loads

The third model briefly recalled here is based on a kinematic approach, in which bricks are supposed to be infinitely resistant and joints are reduced to interfaces with cohesive frictional behavior.

At the microscale, a full description of the model can be given considering a RVE consisting of a central brick and six adjacent bricks. In Fig. 12.7 a RVE is subjected to three elementary in-plane homogenized strains, namely horizontal normal strain (A), shear (B), and vertical normal strain (C). Note that when the RVE is subjected to horizontal in-plane stretching, head and bed joints contribute both to the ultimate strength, whereas in vertical stretching only the bed joints experience a nonvanishing jump in displacement.

The real continuum is replaced by a standard 2D Cauchy continuum, identified by its midplane S of normal $\mathbf{e}_3$. The homogenization procedure is a so-called "compatible identification," which is based on the equality of the internal power dissipated in the 3D discrete system and in the equivalent 2D continuum.

The velocity at any point $\boldsymbol{\xi}$ of one of the bricks (A) is expressed in terms of velocity ($\mathbf{v}^{C^A}$) of the brick centroid, C^A, and rotation rate of the brick ($\boldsymbol{\Phi}^A$).

When $\boldsymbol{\xi}$ lays on any interface between two contiguous bricks A and B, its velocity can be expressed in terms of kinematic unknowns of both bricks as follows:

$$\begin{aligned} \mathbf{v}^A(\boldsymbol{\xi}) &= \mathbf{v}^{C^A} + \mathbf{M}(\boldsymbol{\Phi}^A)(\boldsymbol{\xi} - \mathbf{C}^A) \\ \mathbf{v}^B(\boldsymbol{\xi}) &= \mathbf{v}^{C^B} + \mathbf{M}(\boldsymbol{\Phi}^B)(\boldsymbol{\xi} - \mathbf{C}^B) \end{aligned} \tag{12.15}$$

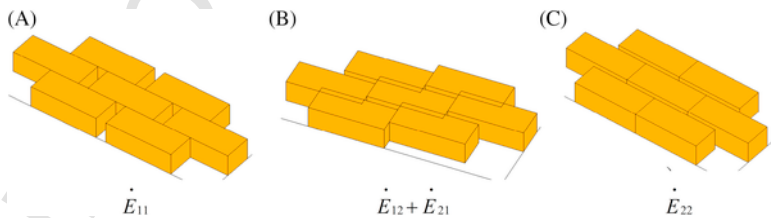

FIGURE 12.7 Deformation modes considered in the compatible identification model.

The jump in velocity $\left[\left[\mathbf{v}(\boldsymbol{\xi})\right]\right]$ at $\boldsymbol{\xi}$ is therefore given by:

$$\begin{aligned}\left[\left[\mathbf{v}(\boldsymbol{\xi})\right]\right] &= \mathbf{v}^A(\boldsymbol{\xi}) - \mathbf{v}^B(\boldsymbol{\xi}) \\ &= \mathbf{v}^{C^A} - \mathbf{v}^{C^B} + \mathbf{M}(\boldsymbol{\Phi}^A)(\boldsymbol{\xi} - \mathbf{C}^A) \\ &\quad - \mathbf{M}(\boldsymbol{\Phi}^B)(\boldsymbol{\xi} - \mathbf{C}^B)\end{aligned} \tag{12.16}$$

The power dissipated at the interface is:

$$\begin{aligned}\pi &= \int_I \left[\mathbf{t}^A(\boldsymbol{\xi}) \cdot \mathbf{v}^A(\boldsymbol{\xi}) + \mathbf{t}^B(\boldsymbol{\xi}) \cdot \mathbf{v}^B(\boldsymbol{\xi})\right] dS \\ &= \int_I \mathbf{t}^A(\boldsymbol{\xi}) \cdot \left[\mathbf{v}(\boldsymbol{\xi})\right] dS\end{aligned} \tag{12.17}$$

where $\mathbf{t}^A(\boldsymbol{\xi}) = \begin{bmatrix}\tau_{13}(\boldsymbol{\xi}) & \tau_{23}(\boldsymbol{\xi}) & \sigma_{33}(\boldsymbol{\xi})\end{bmatrix}^T$ is the stress vector at $\boldsymbol{\xi}$, and $\mathbf{t}^A(\boldsymbol{\xi}) = -\mathbf{t}^B(\boldsymbol{\xi})$.

The velocity of a point $\mathbf{P}=(x_1^P, x_2^P, x_3^P)$ in the equivalent continuum corresponds to the velocity $\mathbf{w}(\mathbf{x}) = (w_1, w_2)=\left(w_1, w_2\right)$ of the point $\mathbf{x} = (x_1^P, x_2^P, 0)$ laying in the midplane of the wall.

The power dissipated in the equivalent continuum is $\pi = \mathbf{N}^T\dot{\mathbf{E}}$, where $\dot{\mathbf{E}} = \begin{bmatrix}\dot{E}_{11} & \dot{E}_{12} + \dot{E}_{21} & \dot{E}_{22}\end{bmatrix}^T$ is the array of the in-plane strain rates, and $\mathbf{N} = \begin{bmatrix}N_{11} & N_{12} & N_{22}\end{bmatrix}^T$ is an array collecting the homogenized membrane forces.

In the so-called compatible identification, the power dissipated in the heterogeneous assemblage of blocks and interfaces is assumed to be equal to that dissipated in the equivalent model.

To this end, fields $\mathbf{w}(\mathbf{x})$ corresponding to possible actual failure mechanisms are a priori chosen as combinations of elementary deformation modes of the unit cell. From a practical point of view, a field $\mathbf{w}(\mathbf{x})$ corresponding to each elementary deformation mode is obtained by alternatively taking one of the macroscopic strain–rate components equal to unity and by setting all the other components equal to zero: $\mathbf{w}(\mathbf{x})$ is then given a simple polynomial expression. Once that $\mathbf{w}(\mathbf{x})$ is known, the rotation rates and velocities of each brick belonging to the RVE in the heterogeneous model are determined, by assuming as point $\mathbf{x}$ the centroid of the brick under examination.

12.5.2 Extension to transverse loads: Reissner–Mindlin model

In the Reissner–Mindlin (RM) plate model the angular velocity ($\boldsymbol{\omega}$) of any segment perpendicular to the midplane is independent of the transverse velocity, w_3. The Compatible Identification approach can be extended to masonry walls obeying the RM model and subjected both to in-plane and transverse loads, by applying suitable homogenized curvature and transverse shear rates, as shown in Figs. 12.8 and 12.9.

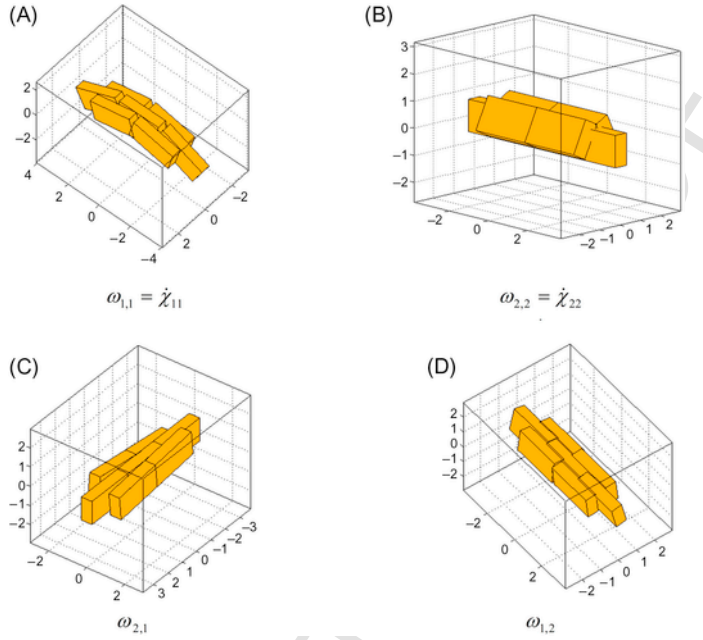

FIGURE 12.8 Elementary homogeneous deformations applied to the representative volume element. (A) $\omega_{1,1} = \dot{\chi}_{11}$; (B) $\omega_{2,2} = \dot{\chi}_{22}$; (C) $\omega_{2,1}$; (D) $\omega_{1,2}$.

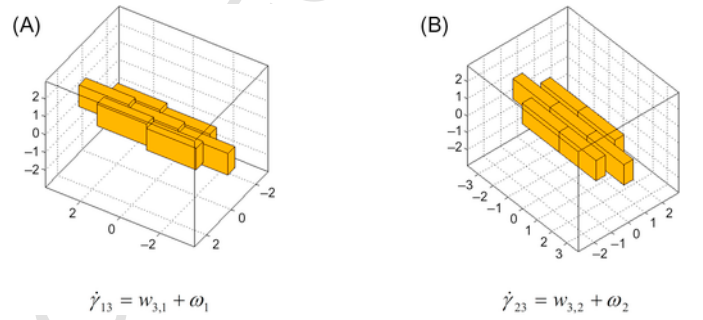

FIGURE 12.9 Shear deformation rates. (A) $\dot{\gamma}_{13}$; (B) $\dot{\gamma}_{23}$.

Fig. 12.8A shows the effect on the brickwork of a homogeneous curvature rate $\dot{\chi}_{11} = \omega_{1,1}$ all the other generalized strains being set to zero. In this case, both head and bed joints are involved in the dissipation induced by this deformation mode.

Fig. 12.8B shows the effect of a homogeneous curvature rate $\dot{\chi}_{22} = \omega_{2,2}$. It is interesting to note that only the bed joints exhibit a jump in velocity between adjacent bricks. Similarly, in Figs. 12.8C and D the cases in which only $\omega_{1,2} \neq 0$, and $\omega_{2,1} \neq 0$ are nonvanishing are examined: combining these two

cases, the deformation mode under homogeneous twisting curvature rate $\dot{\chi}_{12} = \omega_{1,2} + \omega_{2,1}$ can be obtained. In the first case, no bending moment exists in the head joints, whereas bed joints experience twisting. Conversely, in the second case, torsion is present in the head joints and the bed joints experience bending.

Finally, Fig. 12.9 refers to the evaluation of the behavior of masonry under transverse shear strain rates, $\dot{\gamma}_{i3} = w_{3,i} + \omega_i$, i=1,2. In particular, Fig. 12.9A shows the effects of the $\dot{\gamma}_{13}$ component, whereas Fig. 12.9B shows the effects of the $\dot{\gamma}_{23}$ component.

Here, a numerical procedure for obtaining macroscopic homogenized failure surfaces for running bond masonry is presented. The procedure is developed under the hypotheses of RM plate theory, assuming bricks to be infinitely resistant and joints to be reduced to rigid-perfectly plastic interfaces with an associated flow rule.

As the problem is dealt with in the framework of linear programming, for each interface I of area A^I a piecewise linear approximation of the failure surface $\varphi = \varphi(\boldsymbol{\sigma})$ is adopted. The surface is defined by n_{lin} planes of equation $(\mathbf{a}_i^I)^T\boldsymbol{\sigma} = c_i^I \quad 1 \le i \le n_{lin}$, where $\boldsymbol{\sigma} = \begin{bmatrix}\sigma_{33} & \sigma_{13} & \sigma_{23}\end{bmatrix}$, σ_{33} being the normal stress on the interface and σ_{13}, σ_{23} the transverse shear stresses along two perpendicular directions, $\mathbf{a}_i^I$ is a 3×1 vector of the coefficients of the i-th linearization plane, and c_i^I is constant term of the equation of the i-th linearization plane.

Since the jump in velocity at the interfaces is assumed to vary linearly in the discrete model (see Eq. 12.16), for each interface $3\times n_{lin}$ independent plastic multiplier rates are assumed as optimization variables.

At each interface I, the following equality constraints between plastic multiplier rate fields $\dot{\lambda}_i^I(\xi_1, \xi_2)$ and jump in velocity $\left[\mathbf{w}\,(\xi_1, \xi_2)\right]$ are imposed:

$$\left[\mathbf{w}(\xi_1, \xi_2)\right] = \sum_{i=1}^{n_{lin}} \dot{\lambda}_i^I(\xi_1, \xi_2)\frac{\partial \varphi}{\partial \boldsymbol{\sigma}} \tag{12.18}$$

where (ξ_1,ξ_2) is a local reference frame laying on the interface plane, so that ξ_3 is orthogonal to the interface; $\left[\mathbf{w}(\xi_1, \xi_2)\right] = \begin{bmatrix}\Delta w_{33} & \Delta w_{13} & \Delta w_{23}\end{bmatrix}^T$ is the jump in velocity at the I-th interface; any component Δw_{j3} corresponds to the jump along the direction j; $\mathbf{w}$ is linear in (ξ_1,ξ_2); $\dot{\lambda}_i^I(\xi_1, \xi_2)$ is the i-th plastic multiplier rate field of the interface I, associated with the i-th linearization plane of the failure surface; also $\dot{\lambda}_i^I$ is linear in (ξ_1,ξ_2).

Eq. (12.18) is nothing but the specialization, for the interface I, of the well-known normality rule $\dot{\varepsilon}_{ij} = \dot{\lambda}(\partial\phi/\partial\sigma_{ij})$, where $\dot{\varepsilon}_{ij}$ is the plastic strain rate, $\dot{\lambda}$ is the plastic multiplier, and ϕ is the failure surface, which coincides with the plastic potential in the case of associated plasticity.

In order to satisfy Eq. (12.18) at any point of any interface I, nine equality constraints have to be imposed, corresponding to Eq. (12.18) evaluated at three different points $P_k = (\xi_1^{P_k}, \xi_2^{P_k})$ of the interface I. Explicitly:

$$\left[\mathbf{w}(\xi_1^{P_k}, \xi_2^{P_k})\right] = \sum_{i=1}^{n_{lin}} \dot{\lambda}_i^I(\xi_1^{P_k}, \xi_2^{P_k}) \frac{\partial \varphi}{\partial \boldsymbol{\sigma}} \quad k = 1, 2, 3. \tag{12.19}$$

The power dissipated at the I-th interface, defined as the dot product of the interface tractions for the jump in velocity, is evaluated using the following equation:

$$\begin{aligned} \pi_{\text{int}}^I &= \int_{A^I} [\mathbf{w}]^T \boldsymbol{\sigma} \, dA^I \\ &= \int_{A^I} \sum_{i=1}^{n_{lin}} \dot{\lambda}_i^I(\xi_1, \xi_2) \left[\frac{\partial \varphi}{\partial \boldsymbol{\sigma}}\right]^T \boldsymbol{\sigma} \, dA^I \\ &= \frac{1}{3} \sum_{i=1}^{n_{lin}} c_i^I \sum_{k=1}^{3} \dot{\lambda}_i^I(\xi_1^{P_k}, \xi_2^{P_k}) A^I. \end{aligned} \tag{12.20}$$

The external power can be written as $\pi_{ext} = (\boldsymbol{\Sigma}_0^T + \lambda \boldsymbol{\Sigma}_1^T)\mathbf{D}$, where $\boldsymbol{\Sigma}_0$ is the array of the dead loads; λ is the multiplier of the live loads; $\boldsymbol{\Sigma}_1$ is the array gathering the reference values of the live loads (which defines the optimization direction in the space of the macroscopic stresses); and $\mathbf{D}$ is the array of the generalized macroscopic strain rates. $\mathbf{D}$ collects in-plane deformation rates ($\dot{E}_{11}$ $\dot{E}_{12}$ $\dot{E}_{22}$), curvature rates ($\dot{\chi}_{11}$ $\dot{\chi}_{12}$ $\dot{\chi}_{22}$), and transverse shear strain rates ($\dot{\gamma}_{13}$ $\dot{\gamma}_{23}$); see Figs. 12.7–12.9. Introducing the classic normalization condition of the failure mechanism $\boldsymbol{\Sigma}_1^T \mathbf{D} = 1$, the external power becomes linear in $\mathbf{D}$ and λ and can be written as $\pi_{ext} = \boldsymbol{\Sigma}_0^T \mathbf{D} + \lambda$.

The core of the Compatible Identification approach is to assign prescribed microscopic strain-rate periodic velocity fields to the unit cell (represented in Figs. 12.7–12.9). As a consequence, for each interface I a linear relationship can be written between $\mathbf{D}$ and the jump in velocity as follows:

$$\left[\mathbf{w}(\xi_1, \xi_2)\right] = \mathbf{G}^I(\xi_1, \xi_2)\mathbf{D}, \tag{12.21}$$

where $\mathbf{G}^I(\xi_1, \xi_2)$ is a 3×10 matrix that depends only on the geometry of the interface under consideration.

By assembling the equality constraints (12.18)–(12.21), and using the kinematic formulation of classic limit analysis, the following constrained minimization problem is finally obtained to evaluate a point of the failure surface:

$$\begin{cases} \lambda = \min\limits_{\hat{\mathbf{x}}=\left[\mathbf{D},\lambda_i^I(P_k)\right]} \sum_{I=1}^{n^I} \pi_{\text{int}}^I - \boldsymbol{\Sigma}_0^T \mathbf{D} \\ {\boldsymbol{\Sigma}_1}^T \mathbf{D} = 1 \\ \mathbf{G}^I(P_k)\mathbf{D} = \left[\mathbf{w}(P_k)\right] = \sum_{i=1}^{n_{lin}} \lambda_i^I(\xi_1^{P_k}, \xi_2^{P_k}) \dfrac{\partial \varphi}{\partial \boldsymbol{\sigma}} \quad P_k \in I \end{cases} \tag{12.22}$$

where n^I is the total number of interfaces considered and $\hat{\mathbf{x}}$ is the array of all the optimization unknowns. Similar to the homogenization models previously presented in this chapter, problem (12.22) can be easily handled numerically using either one of the well-known simplex and interior point methods, due to the very limited number of optimization unknowns involved. In fact, $\hat{\mathbf{x}}$ collects only $3 \times n_{lin} \times n^I$ plastic multiplier rates and the macroscopic kinematic variables $\mathbf{D}$.

Problem (12.22) is written in general form, as it covers both in-and out-of-plane loads, and allows interaction failure surfaces of masonry to be estimated through a kinematic approach.

Denoting by $\boldsymbol{\Sigma} = (N_{11}, N_{12}, N_{22}, M_{11}, M_{12}, M_{22}, T_{13}, T_{23})$ an array gathering all the generalized stresses, and by $\hat{\Phi}(\boldsymbol{\Sigma})$ the macroscopic failure polytope for masonry, a 2D representation of $\hat{\Phi}$ for any couple of variables Σ_i and Σ_j can be obtained by fixing a direction defined by a unit vector $\mathbf{n}_\Sigma$ in the 8D $\boldsymbol{\Sigma}$ space, so that $\mathbf{n}_\Sigma(i) = \cos\ \psi$ and $\mathbf{n}_\Sigma(j) = \sin\ \psi$ (with $\tan\ \psi = \Sigma_j / \Sigma_i$), and solving the following optimization problem:

$$\begin{cases} \min\{\lambda\} = \sum_{I=1}^{n^I} \pi_{\text{int}}^I - \boldsymbol{\Sigma}_0^T \mathbf{D} \\ {\mathbf{n}_\Sigma}^T \mathbf{D} = 1 \quad \mathbf{n}_\Sigma(i) = \cos\psi \quad \mathbf{n}_\Sigma(j) = \sin\ \psi \\ \mathbf{G}^I(P_k)\mathbf{D} = \left[\mathbf{w}(P_k)\right] = \sum_{i=1}^{n_{lin}} \lambda_i^I(\xi_1^{P_k}, \xi_2^{P_k}) \dfrac{\partial \varphi}{\partial \boldsymbol{\sigma}} \end{cases} \tag{12.23}$$

where λ denotes the load multiplier for a prescribed radial load path in the $(\Sigma_i, \Sigma_j$; see also Fig. 12.2); i and j denote the axes of projection of $\hat{\Phi}$.

12.6 METHOD OF CELLS: A METHOD OF CELLS-TYPE APPROACH

12.6.1 Homogenized yield surface under in-plane loads

The so-called MoC was originally proposed by Aboudi (1991) for unidirectional composites reinforced by a regular pattern of long, parallel fibers. The MoC has been recently extended to masonry by Taliercio (2014, 2016) to evaluate in closed form the macroscopic elastic and creep coefficients, and by Milani and Taliercio (2015, 2016) to estimate macroscopic strength domains. The method, applied to running- or header-bond, consists of subdividing the unit cell into rectangular subcells, as shown in Fig. 12.10A. In each subcell, the velocity field is approximated using two sets of strain rate-periodic, piece-

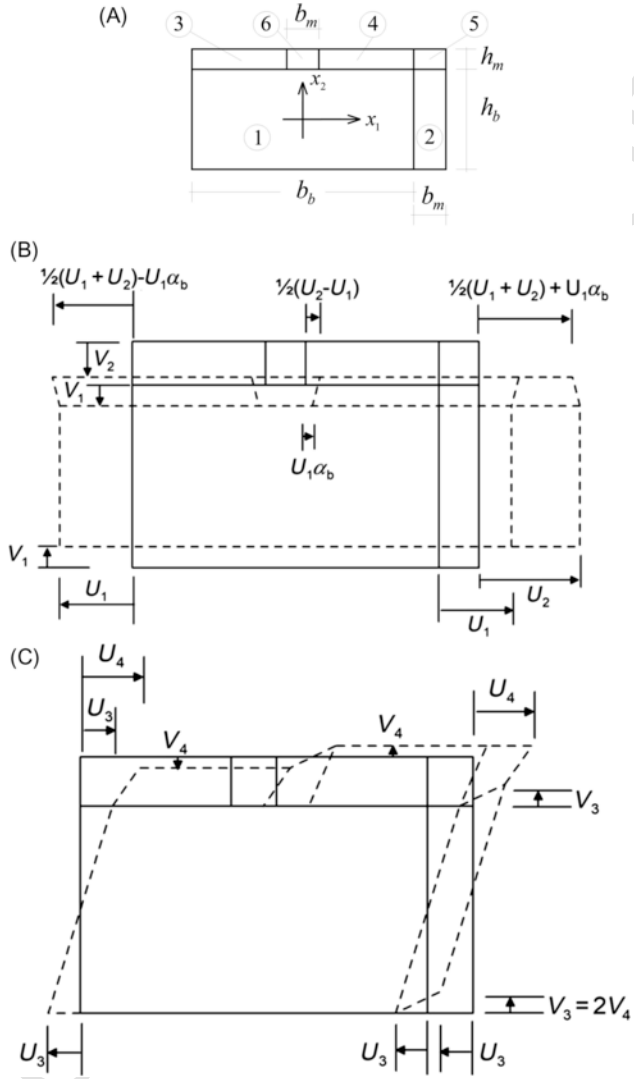

FIGURE 12.10 (A) RVE adopted in the MoC-type approach and subdivision into subcells. (B and C) Strain-periodic kinematically admissible velocity field under horizontal or vertical macroscopic stresses (A) and shear (B).

wise-differentiable velocity fields: one for normal deformation modes and one for a shear-type deformation mode.

Denting by $u_1^{(i)}$ and $u_2^{(i)}$ the horizontal and vertical velocity fields in the *i*-th cell, under macroscopic vertical and horizontal normal strains (Fig. 12.10,B)

the velocities inside each subcell are given by:

$$u_1^{n(1)} = 2U_1\frac{x_1}{b_b} \quad u_2^{n(1)} = -2V_1\frac{x_2}{h_b}$$

$$u_1^{n(2)} = U_1 + \frac{(U_2-U_1)\left(x_1-\frac{b_b}{2}\right)}{b_m} \qquad u_2^{n(2)} = u_2^{n(1)}$$

$$u_1^{n(3)} = u_1^{n(1)} - \frac{(U_1(1+2\alpha_b)-U_2)\left(\frac{h_b}{2}-x_2\right)}{2h_m} \quad u_2^{n(3)} = -V_1 + \frac{(V_1-V_2)\left(x_2-\frac{h_b}{2}\right)}{h_m}u_2^{n(1)}$$

$$u_1^{n(4)} = u_1^{n(1)} + \frac{(U_1(1+2\alpha_b)-U_2)\left(\frac{h_b}{2}-x_2\right)}{2h_m} \qquad u_2^{n(4)} = u_2^{n(3)}$$

$$u_1^{n(5)} = U_1 - \frac{(U_1(1+2\alpha_b)-U_2)\left(\frac{b_b+b_m}{2}-x_1\right)\left(x_2-\frac{h_b}{2}\right)}{b_m h_m} - \frac{(U_1-U_2)\left(x_1-\frac{b_b}{2}\right)}{b_m} \tag{12.24}$$

$$u_2^{n(5)} = -V_2\frac{x_2-\frac{h_b}{2}}{h_m} - V_1\frac{\left(\frac{h_b}{2}+h_m-x_2\right)}{h_m}$$

$$u_1^{n(6)} = 2\frac{x_1}{b_b}\left(U_1 - \frac{\left(U_1+\frac{U_1-U_2}{2\alpha_b}\right)\left(x_2-\frac{h_b}{2}\right)}{h_m}\right) \quad u_2^{n(6)} = -V_1 + \frac{(V_1-V_2)\left(x_2-\frac{h_b}{2}\right)}{h_m}$$

The fields in Eq. (12.24) depend on four DOFs, U_1, U_2, V_1, and V_2, with a clear physical meaning as shown in Fig 12.10B. The reference system (x_1,x_2) and the meaning of the geometrical parameters h_b, b_b, etc., is provided in Fig. 12.10A. $\alpha_b = b_m/b_b$ is the ratio of the bed joint thickness to the brick height. It is interesting to note that the velocity fields inside each subcell are either linear (cells 1, 3, 4) or bilinear (cells 2, 5, 6).

When a shear deformation mode is applied to the RVE, the velocity fields in the subcells are expressed as:

$$u_1^{t(1)} = 2U_3\frac{x_2}{h_b} \quad u_2^{t(1)} = 0 \quad u_1^{t(2)} = u_1^{t(1)} \quad u_2^{t(2)} = V_3\frac{x_1-\frac{b_b}{2}}{b_m}$$

$$u_1^{t(3)} = U_3 + \frac{U_4-U_3}{h_m}\left(x_3-\frac{h_b}{2}\right) \quad u_2^{t(3)} = -V_4\frac{x_2-\frac{h_b}{2}}{h_m}$$

$$u_1^{t(4)} = u_1^{t(3)} \quad u_2^{t(4)} = -u_2^{t(3)} \tag{12.2}$$

$$u_1^{t(5)} = u_1^{t(3)} \quad u_2^{t(5)} = -V_3\frac{\left(x_1-\frac{b_b+b_m}{2}\right)\left(x_2-\frac{h_b}{2}\right)-h_m\left(x_1-\frac{b_b}{2}\right)}{b_m h_m}$$

$$u_1^{t(6)} = u_1^{t(3)} \quad u_2^{t(6)} = V_3\frac{x_1\left(x_2-\frac{h_b}{2}\right)}{b_m h_m}$$

In Eq. (12.25) the symbols $u_1^{t(i)}$ and $u_2^{t(i)}$ denote the horizontal and vertical velocity fields in the *i*-th subcell under macroscopic shear. The meanings of the three independent DOFs, U_3, U_4, and V_3, are shown in Fig. 12.10C ($V_4 = V_3/2$).

The velocity field over the RVE under any macroscopic strain can be expressed as the sum of Eqs. (12.24) and (12.25), that is, $u_1^{(i)} = u_1^{n(i)} + u_1^{t(i)}$ and $u_2^{(i)} = u_2^{n(i)} + u_2^{t(i)}$ where the superscript (*i*) indicates the (*i*)-th subcell.

At each point of any subcell, the associated flow rule corresponds to three equality constraints. Denoting by $\dot{\boldsymbol{\varepsilon}}_{pl}^{(i)}$ the plastic strain rate in the (*i*)-th subcell, the flow rule can be written as

$$\dot{\varepsilon}_{pl}^{(i)} = \left[\frac{\partial u_1^{(i)}}{\partial x_1} \quad \frac{\partial u_2^{(i)}}{\partial x_2} \quad \frac{\partial u_1^{(i)}}{\partial x_2} + \frac{\partial u_2^{(i)}}{\partial x_1}\right] = \dot{\lambda}^{(i)} \frac{\partial S^{b,m}}{\partial \boldsymbol{\sigma}},$$

where $\dot{\lambda}^{(i)}$ ($\geq$0) is the plastic multiplier and $S^{b,m}$ is the (non) linear yield surface of either bricks (*b*) or mortar (*m*).

As outlined in the preceding paragraphs, the yield surfaces of bricks and mortar are usually linearized by *m* planes, so that each strength criterion is defined by a set of linear inequalities of the form $S^{b,m} \equiv \mathbf{A}^{in}\boldsymbol{\sigma} \leq \mathbf{b}^{in}$. As $\dot{\boldsymbol{\varepsilon}}_{pl}^{(i)}$ varies at most (bi-)linearly within each subcell, plastic admissibility is checked only at three of the corners. Hence, nine linear equality constraints per subcell are introduced in matrix form as $\mathbf{A}_{U(i)}^{eq}\mathbf{U} + \mathbf{A}_{\lambda(i)}^{eq}\dot{\boldsymbol{\lambda}}^{(i)} = 0$, where $\mathbf{U}$ is an array collecting the 7 DOFs describing any microscopic velocity field (i.e., $\boldsymbol{U}$={U_1, U_2, U_3, U_4, V_1, V_2, V_3}^{T}), $\dot{\boldsymbol{\lambda}}^{(i)} = \left[\dot{\boldsymbol{\lambda}}_A^{(i)T} \quad \dot{\boldsymbol{\lambda}}_B^{(i)T} \quad \dot{\boldsymbol{\lambda}}_C^{(i)T}\right]^T$ is an array of 3 *m* entries, collecting the rates of the plastic multipliers $\dot{\boldsymbol{\lambda}}_J^{(i)}$ at three of the corners of the rectangular subcell (*J*=*A*, *B*, *C*), and $\mathbf{A}_{U(i)}^{eq}$, $\mathbf{A}_{\lambda(i)}^{eq}$ are a 9×7 and a 9×3 *m* matrix, respectively. The plastic admissibility conditions are then assembled cell by cell, leading to the following system of equality constraints:

$$\mathbf{A}_U^{eq}\mathbf{U} + \mathbf{A}_\lambda^{eq}\dot{\boldsymbol{\lambda}} = 0 \tag{12.26}$$

where $\mathbf{A}_U^{eq} = \left[\mathbf{A}_{U(1)}^{eq\,T} \quad \cdots \quad \mathbf{A}_{U(6)}^{eq\,T}\right]^T$, $\dot{\boldsymbol{\lambda}} = \left[\dot{\boldsymbol{\lambda}}^{(1)T} \quad \cdots \quad \dot{\boldsymbol{\lambda}}^{(6)T}\right]^T$, and $\mathbf{A}_\lambda^{eq}$ is a (6·9)×(6·3 *m*) block matrix, which can be expressed as:

$$\mathbf{A}_\lambda^{eq} = \mathbf{A}_{\lambda(1)}^{eq} \oplus \mathbf{A}_{\lambda(2)}^{eq} \oplus \cdots \oplus \mathbf{A}_{\lambda(6)}^{eq}; \tag{12.27}$$

the symbol $\oplus$ denotes direct sum.

Let *B* and *C* be a couple of corners at the opposite ends of one of the diagonals of the (*i*)-th rectangular subcell. The internal power dissipated within the subcell can be written as:

$$\begin{aligned}\pi_{in}^{(i)} &= \frac{\Omega^{(i)}}{2}\left(\mathbf{b}_{in}^{(i)T}\dot{\boldsymbol{\lambda}}_B^{(i)} + \mathbf{b}_{in}^{(i)T}\dot{\boldsymbol{\lambda}}_C^{(i)}\right) \\ &= \frac{\Omega^{(i)}}{2}\begin{bmatrix}\mathbf{0}_{1\times m} & \mathbf{b}_{in}^{(i)T} & \mathbf{b}_{in}^{(i)T}\end{bmatrix}\dot{\boldsymbol{\lambda}}^{(i)},\end{aligned} \tag{12.28}$$

where $\mathbf{0}_{1\times m}$ is an array of m zero entries and $\Omega^{(i)}$ is the area of the (i)-th subcell. The power dissipated inside the whole RVE is obtained as the sum of the contributions of the single subcells:

$$\pi_{in} = \sum_{i=1}^{6}\frac{\Omega^{(i)}}{2}\begin{bmatrix}\mathbf{0}_{1\times m} & \mathbf{b}_{in}^{(i)T} & \mathbf{b}_{in}^{(i)T}\end{bmatrix}\dot{\boldsymbol{\lambda}}^{(i)}. \tag{12.29}$$

The "external load" applied to the RVE is the macroscopic stress, corresponding to a point of the homogenized failure surface. The array of the macroscopic stress components can be expressed as $\boldsymbol{\Sigma} = \lambda\begin{bmatrix}\alpha & \beta & \gamma\end{bmatrix}^T$, where λ is a load multiplier and α, β, γ are, as usual, the director cosines defining the direction of $\boldsymbol{\Sigma}$ in the space of the homogenized in-plane stresses. Accordingly, the power of the external loads can be written as:

$$\pi_{ex} = \lambda\begin{bmatrix}\alpha & \beta & \gamma\end{bmatrix}\mathbf{D} \tag{12.30}$$

In limit analysis a normalization condition is needed because the shape of the failure mode is identified, but its amplitude is undetermined:

$$\begin{bmatrix}\alpha & \beta & \gamma\end{bmatrix}\mathbf{D} = 1 \tag{12.31}$$

In the framework of the upper bound theorem of limit analysis, any point of the homogenized failure surface is determined by using following constrained minimization problem:

$$\text{subject to}\begin{cases}\text{Find}\min \pi_{in} \\ \begin{bmatrix}\alpha & \beta & \gamma\end{bmatrix}\mathbf{D} = 1 & (a) \\ \mathbf{A}_U^{eq}\mathbf{U} + \mathbf{A}_\lambda^{eq}\dot{\boldsymbol{\lambda}} = \mathbf{0} & (b) \\ \mathbf{D} = \frac{1}{A}\int_{\partial Y}^{s}\mathbf{v}\otimes\mathbf{n}dS & (c) \\ \dot{\boldsymbol{\lambda}} \geq \mathbf{0} & (d)\end{cases} \tag{12.32}$$

where Eq. (12.32a) is the normalization condition (12.31); Eq. (12.32b) is the set of equations representing the admissibility of the plastic flow, Eq. (12.26); and Eq. (12.32c) links the homogenized strain rate with the local velocity field.

12.6.2 Extension to transverse loads

Under transverse loads, the wall is supposed to behave as a Kirchhoff–Love plate. Hence, only the transverse velocity field, $w(x_1,x_2)$, has to considered.

Assuming the wall undergoes bending moments acting about the head joints (M_{xx}) and/or about the bed joints (M_{yy}), it is possible to define a C^1-type transverse velocity field defined by four parameters (or DOF, $W_1 \ldots W_4$) as follows:

$$w_n^{(12.1)} = \frac{4W_1 x_1^2}{b_b^2} + \frac{4W_2 x_2^2}{h_b^2}, \tag{12.33a}$$

$$w_n^{(2)} = w_n^{(1)} + 4\frac{W_3\left(-\frac{b_b}{2} + x_1\right)^2}{\left(b_b - b_m\right) b_m} \tag{12.33b}$$

$$w_n^{(3)} = w_n^{(1)} + \frac{W_4\left(h_b - 2x_2\right)^2}{8h_m^2} - \frac{W_3\left(b_b + b_m + 4x_1\right)\left(h_b - 2x_2\right)^2\left(h_b + 3h_m - 2x_1\right)}{4\left(b_b - b_m\right)h_m^3} \tag{12.33c}$$

$$w_n^{(4)} = w_n^{(1)} + \frac{W_4\left(h_b - 2x_2\right)^2}{8h_m^2} - \frac{W_3\left(b_b + b_m - 4x_1\right)\left(h_b - 2x_2\right)^2\left(h_b + 3h_m - 2x_2\right)}{4\left(b_b - b_m\right)h_m^3} \tag{12.33d}$$

$$w_n^{(5)} = w_n^{(1)} + \frac{W_4\left(h_b - 2x_2\right)^2}{8h_m^2} + W_3\left(1 - \frac{2\left(b_b - 2x_1\right)}{b_b - b_m}\right) + \left(\frac{\left(b_b{}^2 + b_b\left(b_m -\right.\right.\right.$$

$$w_n^{(6)} = w_n^{(1)} + \frac{W_4\left(h_b - 2x_2\right)^2}{8h_m^2} - \frac{W_3\left(b_b b_m - 4x_1^2\right)\left(h_b - 2x_2\right)^2\left(h_b + 3h_m - 2x_2\right)}{4\left(b_b - b_m\right)b_m h_m^3} \tag{12.33f}$$

For the sake of clarity, Fig. 12.11 shows a wall deformed according to the previous equation assuming W_1=W_2=W_4=0. Zoomed details of the deformed wall are also shown in subfigures (B) and (C), to highlight twisting in the bed joints.

When the RVE is subjected to torsion (M_{12}=M_{21}), a C^0-type piecewise differentiable velocity field defined only by two parameters W_5 and W_6 is assumed:

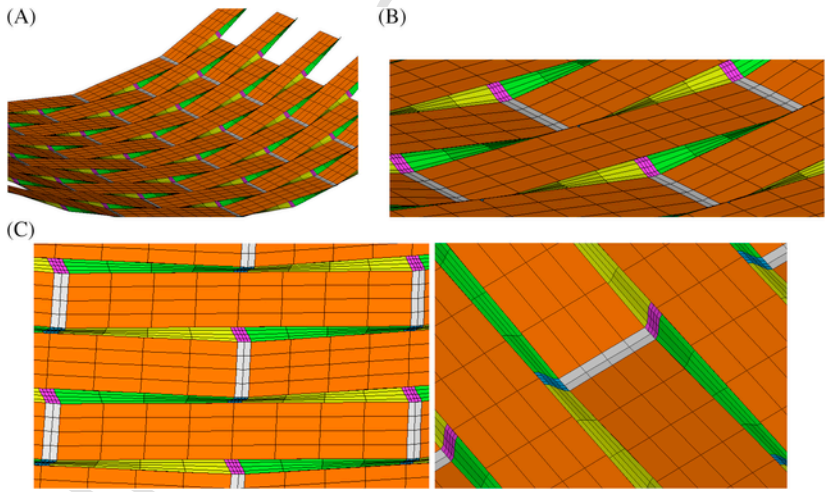

FIGURE 12.11 (A) Deformed masonry wall subjected to bending curvature about the head joints and (B) details of a deformed REV. (C) Details of mortar joints deformation. Brick deformation is neglected.

$$w_t^{(12.1)} = \frac{4W_5 x_1 x_2}{b_b h_b} \tag{12.34a}$$

$$w_t^{(2)} = w_t^{(1)} + \frac{2W_6\left(-\frac{b_b}{2} + x_1\right)x_1 x_2}{b_m h_b} \tag{12.34b}$$

$$w_t^{(3)} = w_t^{(1)} - W_6\frac{\left(\left(b_b + b_m\right)h_b + 4\left(h_b + h_m\right)x_1\right)\left(h_b - 2x_2\right)}{4\left(b_b + b_m\right)h_b h_m} \tag{12.34c}$$

$$w_t^{(4)} = w_t^{(1)} + W_6\frac{\left(\left(b_b + b_m\right)h_b - 4\left(h_b + h_m\right)x_1\right)\left(h_b - 2x_2\right)}{4\left(b_b + b_m\right)h_b h_m} \tag{12.34d}$$

$$w_t^{(5)} = w_t^{(1)} + W_6\frac{h_b\left(b_m h_b - b_b\left(h_b + 2h_m\right)\right)\left(b_b + b_m - 2x_1\right)}{4b_m\left(b_b + b_m\right)h_b h_m} + 2W_6\frac{b_b\left(b_b h_b \cdot\right.}{}$$

$$w_t^{(6)} = w_t^{(1)} - W_6\frac{\left(b_b h_b - b_m\left(h_b + 2h_m\right)\right)x_1\left(-\frac{h_b}{2} + x_2\right)}{b_m\left(b_b + b_m\right)h_b h_m} \tag{12.34f}$$

Fig. 12.12A and B show a wall deformed under torsion and neglecting brick deformation (W_5=0). Some details of the deformed shape are shown in Fig. 12.12C and D to show how joints are subjected to twisting.

The procedure to estimate a point belonging to the out-of-plane homogenized failure surface is identical to that used for the in-plane case, and is omitted for the sake of brevity. It is only worth noting that, after a suitable assemblage of the constraints, the constrained minimization problem can be written as follows:

$$\min\ \Pi_{in}\left\{\text{subject to}\left\{\begin{array}{ll}\begin{bmatrix}\alpha & \beta & \gamma\end{bmatrix}\dot{\mathbf{X}} = 1 & (a)\\ \mathbf{A}_W^{eq}\mathbf{W} + \mathbf{A}_{\dot{\lambda}}^{eq}\dot{\boldsymbol{\lambda}} = \mathbf{0} & (b)\\ \dot{\mathbf{X}}x_3 = \frac{1}{|\Gamma|}\int_{\Gamma}^{s}\mathbf{v}\otimes\mathbf{n}\,dS & (c)\\ \dot{\boldsymbol{\lambda}} \geq \mathbf{0} & (d)\end{array}\right.\right. \tag{12.35}$$

where Eq. (12.35a) is the normalization condition, Eq. (12.35b) is the set of equations representing the admissibility of the plastic flow, and Eq. (12.35c) relates the homogenized strain rate with the local velocity field.

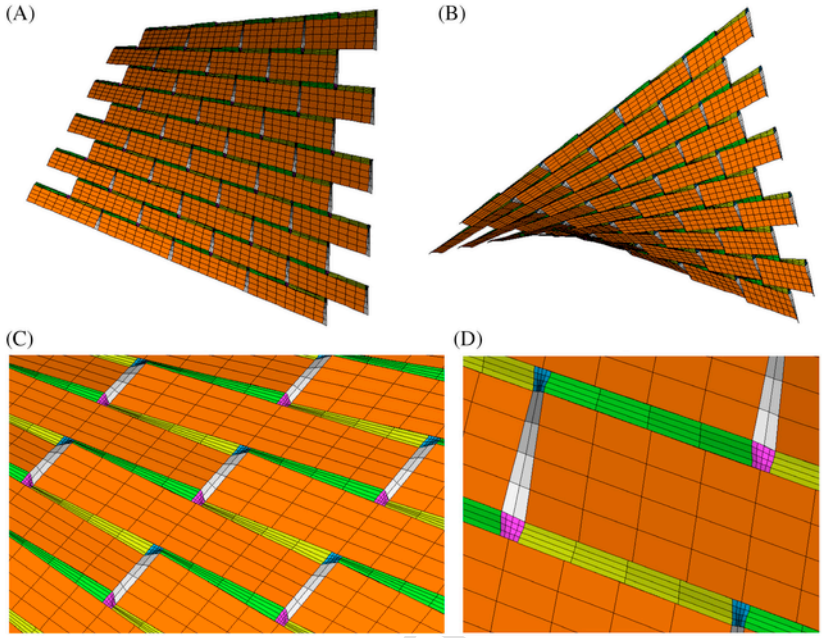

FIGURE 12 (A and B) Deformed masonry wall subjected to twisting. (C) Detail of two deformed RVEs. (D) Detail of joints deformed shape. Brick deformation is neglected.

Note that the independent variables entering the optimization problem (12.35) are the three components of the macroscopic curvature rate $\dot{\boldsymbol{\chi}}$, the plastic multipliers $\dot{\boldsymbol{\lambda}}$, and the six DOFs defining the microscopic velocity field. Via the normalization condition, and equating the internal power dissipation to the power of the external loads, it can be easily shown that the collapse multiplier λ is equal to $\min \Pi_{in}$.

12.7 HOMOGENIZED STRENGTH DOMAINS: IN-PLANE LOADED MASONRY

Some case studies are considered in this section in order to evaluate the capabilities and the limitations of the four limit analysis homogenization strategies considered in this chapter.

First, the lower bound convergence of the PES model as the degree of the approximating polynomials increases is discussed for running bond masonry made of common Italian clay bricks ($250\times120\times55$ mm^3), with 10 mm-thick joints. The mechanical properties are listed in Table 12.1.

Convergence of the model to the actual solution was demonstrated in Milani et al. (2006a), to which readers are referred to for further details. Obviously convergence occurs from the safe side, as the PES model is based on a

TABLE 12.1 Plane-stress Mohr–Coulomb mechanical properties adopted for joints to test the PES model (bricks are assumed to be infinitely resistant).

Friction angle, Φ	Cohesion, c
36°	0.1 MPa
$f_t = \frac{2c\ \cos(\Phi)}{1+\sin(\Phi)}$	$f_c = \frac{2c\ \cos(\Phi)}{1-\sin(\Phi)}$

static approach. In Fig. 12.13A comparison with a standard elasto-plastic FE solution is provided in the tension–tension region, assuming one of the principal stresses, Σ_h, to be parallel to the bed joints.

It can be noted that both the P3 and P4 models match the FE results fairly well, whereas for P0 orthotropy at failure is completely lost. Due to the boundary conditions to be imposed over the RVE, the results for P1 coincide with those given by P0. As the P3 model is sufficiently accurate, from here onward it will be used for comparison with the other models discussed in the chapter.

For all models, the mechanical properties adopted are those summarized in Table 12.1. When joints are reduced to interfaces, that is, for the lower bound CST discretization and the Compatible Identification approach, a Mohr–Coulomb failure criterion with tension (f_t) and compression (f_c) cutoff is adopted for the interfaces. The values assumed for f_t and f_c are reported in Table 12.1, and were obtained from the friction angle Φ and the cohesion c adopted in the PES and MoC models (i.e., with thick joints in plane-stress conditions). Fig. 12.14 shows the homogenized failure surfaces obtained with

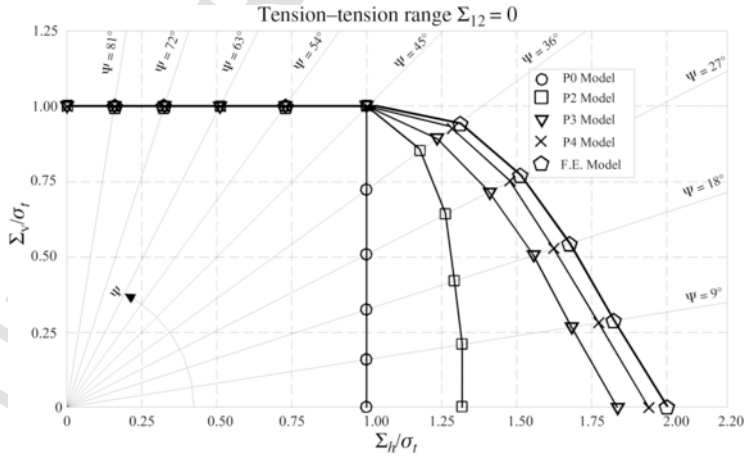

FIGURE 12.13 PES model, convergence of the different polynomial expansions masonry material of Table 12.1 and direction of the principal axes parallel to that of material axes (ϑ=0°, Σ_h=Σ_{11}, Σ_v=Σ_{22}).

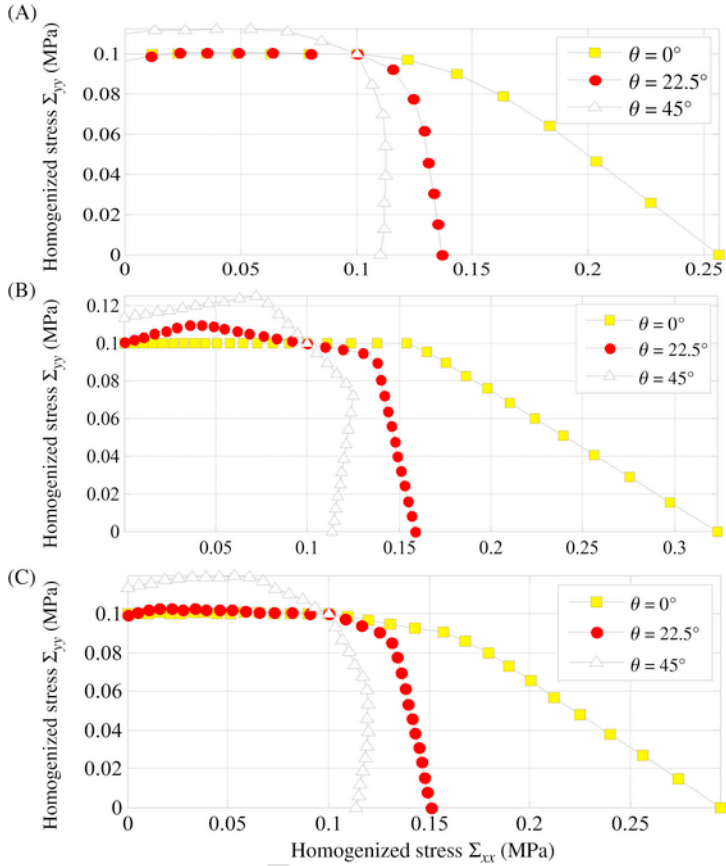

FIGURE 12.14 Comparison among the different homogenization models proposed in the tension–tension region for the masonry material of Table 12.1. (A) PES, P3 approach; (B) equilibrated CST discretization and Compatible Identification model; (C) MoC model ($\Sigma_{xx}=\Sigma_{11}$, $\Sigma_{yy}=\Sigma_{22}$).

the four models, at three orientations ϑ of the bed joints to one of the macroscopic principal stresses (0 degree, 22.5 degree, and 45 degree). In particular, subfigure (A) refers to the PES (P3) approach; (B) to the CST equilibrated model and the compatible identification model (which provide the same results); and (C) to the MoC-type approach. Note that, as the models to which Fig. 12.14B refer give in principle a lower and an upper bound to the real macroscopic strength domain, for brickwork consisting of rigid units and infinitely thin joints the exact solution is obtained.

Fig. 12.14 points out the considerable dependence of the homogenized yield surfaces from the joint thickness (compare, for instance, subfigures (C) and (B)). Thick joints give smoother and nonlinear yield surfaces. Conversely,

if joints are reduced to interfaces, multilinear yield surfaces are obtained, as predicted by de Buhan and de Felice (1997).

The maximum horizontal strength is obtained at ϑ=0 degree, but is much lower in the case of thick joints (0.26 MPa) than in the case of infinitely thin joints (0.31 MPa), the percentage difference being of the order of 15%.

When joints are reduced to interfaces in the MoC model, the theoretical predictions match those given by the compatible identification (or CST equilibrated model; see Fig. 12.16A and B): this is a proof of the good predictive capabilities of the MoC.

As the MoC approach and the PES are the only two models capable of taking the finite joint thickness into account, and as they give, respectively, upper and lower bounds to the real macroscopic strength domain of masonry, it is interesting to assess the convergence of both models to the exact solution. Referring to the same example as before, the results shown in Fig. 12.15 are obtained. It can be noted that P2 is rather inaccurate, whereas P3, as already pointed out, provides acceptable results from an engineering standpoint (also in terms of numerical efficiency). The actual macroscopic yield surface is somewhere between the results given by P4 and the MoC, so that the exact strength domain can be quite strictly bounded. The highest discrepancy occurs at ϑ=0 degree and ψ=arctg(Σ_{22}/Σ_{11})=0 degree, the difference between the strength predicted by the MoC and PES-P4 being of about 5%—a result that is fully satisfactory for practical purposes.

Replacing joints by interfaces, the homogenized strength under horizontal stretching increases to about 0.32 MPa, and the kinematic Compatible Identification approach provides everywhere results that are superimposable to those given by the static CST approach: this means that the exact solution is captured by both models (see Fig. 12.16A and B).

In Fig. 12.16C, the collapse deformation mode of the RVE predicted by the MoC is also represented at ϑ=0 degree and ψ=0 degree. Similar to the predictions of all the alternative homogenization models, it can be noted that head joints are subjected to simple tension, whereas bed joints undergo pure shear. Cross-joints, conversely, exhibit a mixed failure mode, but it does not affect the ultimate homogenized strength significantly, due to their negligible size.

12.8 HOMOGENIZED STRENGTH DOMAINS: OUT-OF-PLANE LOADED MASONRY

In this section, the performances of the different models in the case of transversally loaded masonry are discussed.

First of all, the PES and CST models are applied to the prediction of the ultimate uniaxial bending moment of wallettes loaded in four-point bending, with a bending moment acting about an axis that forms an angle ϑ with respect to the bed joints. The results are shown in Fig. 12.17 and compared with experimental data (Gazzola et al., 1985) and numerical results (Lourenço, 1997)

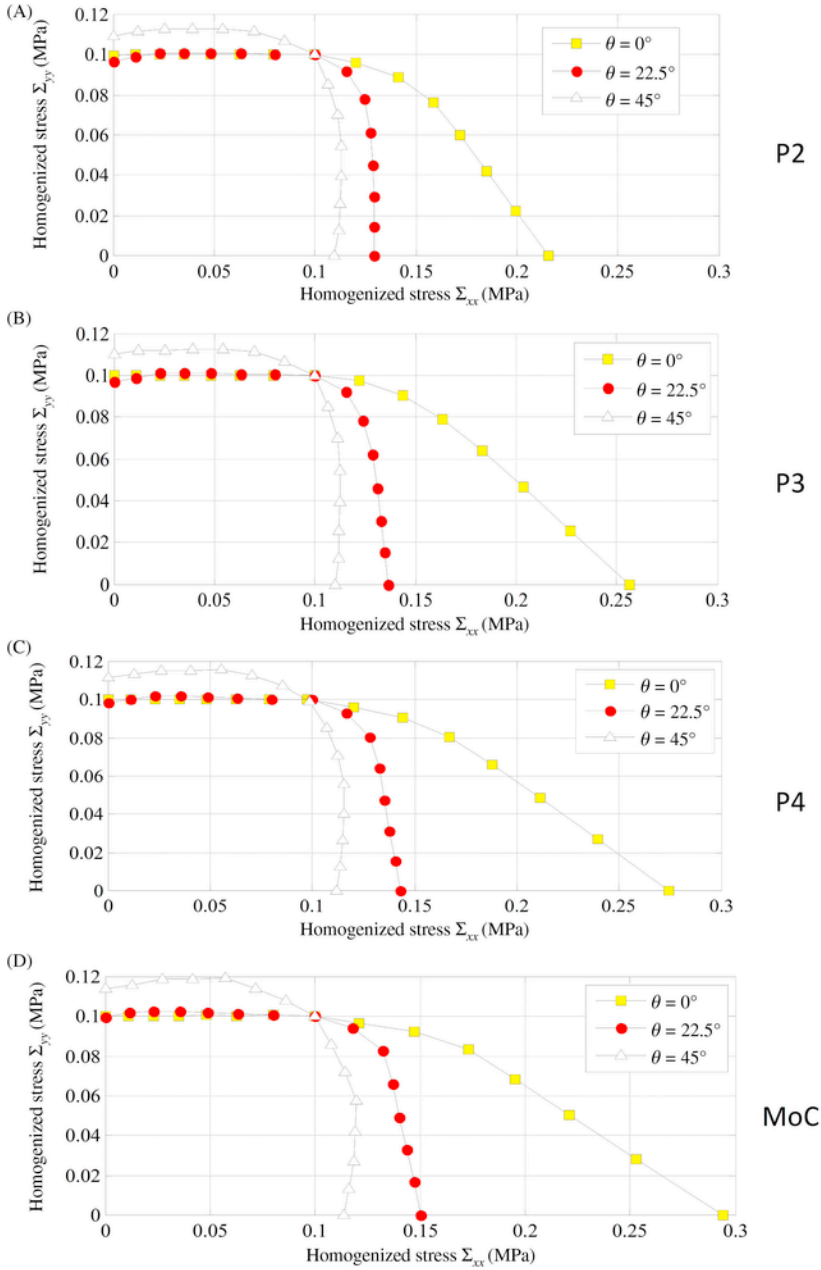

FIGURE 12.15 Comparison between polynomial lower bound approximation and MoC in the tension–tension region, mechanical properties of Table 12.1 ($\Sigma_{xx}=\Sigma_{11}$, $\Sigma_{yy}=\Sigma_{22}$).

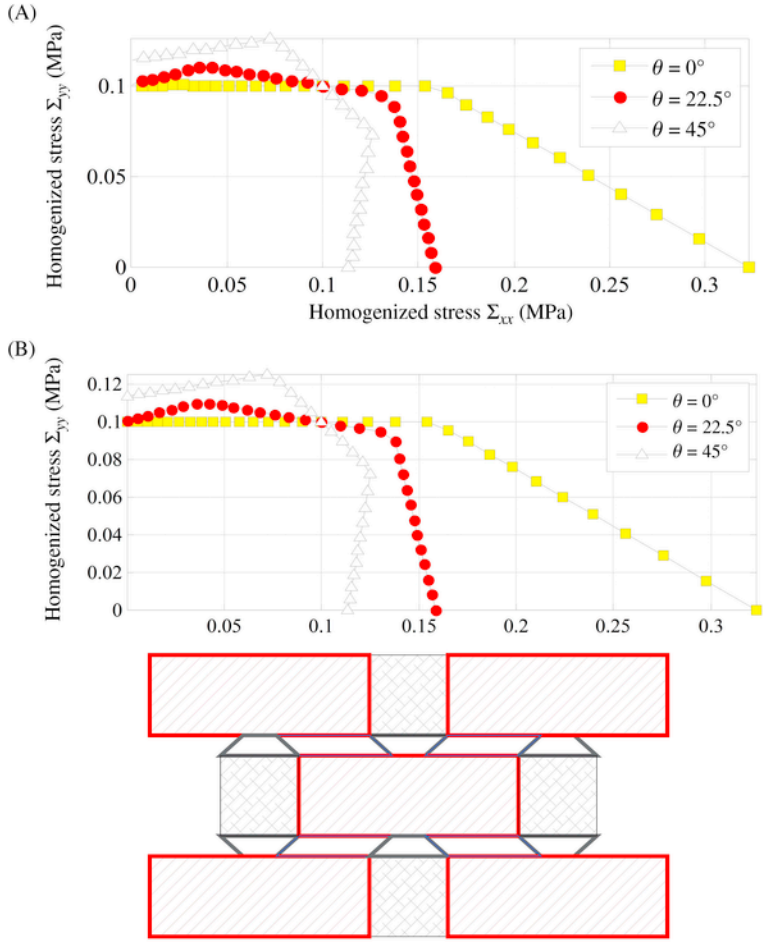

FIGURE 12.16 Comparison between two different homogenization models proposed in the tension–tension region for a masonry element with the properties listed in Table 12.1 and joints reduced to interfaces. (A) Equilibrated CST discretization and Compatible Identification model ($\Sigma_{xx}=\Sigma_{11}$, $\Sigma_{yy}=\Sigma_{22}$); (B) MoC model; (C) MoC deformed shape for horizontal stretching.

with a macroscopic elasto-plastic orthotropic model: subfigure (A) refers to the PES model and subfigure (B) to the CST model. On the vertical axis, the flexural strength, computed as the ultimate bending moment divided by $t^2/6$, is reported: a fictitious linear elastic triangular distribution of the stress across the thickness is assumed.

The input data adopted for the constituent materials are slightly different between PES and CST (as can be seen at $\vartheta=0$ degree, where the flexural strength of masonry is that of the bed joint). As a matter of fact, a slight update of the input data was implemented for the CST model, due to a more re-

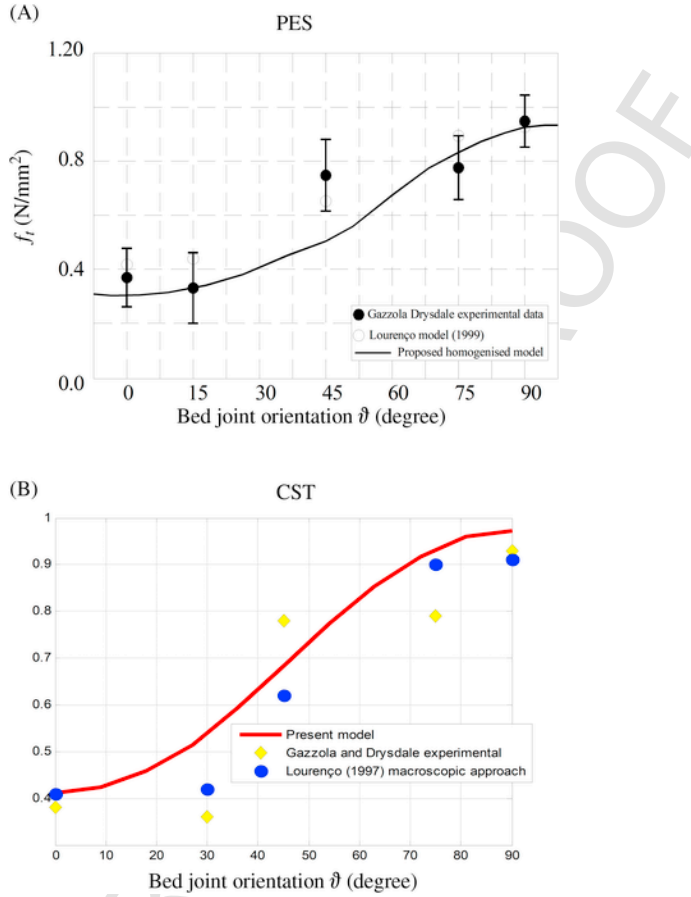

FIGURE 12.17 Comparison among experimental results by Gazzola et al. (1985), plasticity model by Lourenço (1996) and PES (A) or CST (B) in uniaxial bending, at different orientations ϑ of the bed joints to bending moment axis.

fined analysis of the experimental literature available. Interested readers are referred to Milani et al. (2006c) and Milani and Tralli (2011) for further details. Nevertheless, three main issues are worth noting: (1) the rather good experimental data fitting; (2) the capability to reproduce the anisotropic behavior under out-of-plane loads correctly; and (3) the slight overestimation of the strength with the CST model, which is a consequence of the reduction of joints to interfaces.

Consider now the homogenized biaxial flexural behavior. Assume joints to be interfaces obeying a classic Mohr–Coulomb failure criterion. If the wall is sufficiently thin, the Compatible Identification model reduces to a Kirchhoff–Love plate model, for which an analytical solution due to Sab (2003) is avail-

able in the absence of twisting moments. Provided that the number of layers into which the wall thickness is divided is sufficiently high, the safe approximations given by the CST and PES models match quite well the analytically predicted orthotropic multilinear failure surface. It is found that a subdivision into 10 layers is suitable for both the PES (Fig. 12.18) and the CST (Fig. 12.19) model. This applies also in presence of a twisting moment: in Fig. 12.19B the results obtained with the CST model are compared with those obtained by the Compatible Identification approach in the horizontal bending-twisting moment plane (M_{11},M_{12}), for different numbers of layers across the wall thickness.

The results presented so far were obtained in the absence of vertical membrane compressive loads (N_{22}=0), a situation which occurs only in laboratory tests on small-size walls. In this case, no perceivable difference is observed between results provided by the models with joints obeying a Mohr–Coulomb failure criterion with and without compression cap, as the compressive strength of masonry has little effects under pure bending.

For practical purposes, it is more interesting to predict the flexural strength of masonry in presence of vertical compressive loads. Let us consider again a running bond masonry built with common Italian clay bricks and joints reduced to interfaces obeying a Mohr–Coulomb failure criterion with tension cutoff and linear compressive cap; its mechanical properties are listed in Table 12.2. Homogenized out-of-plane yield surfaces are evaluated at fixed, increasing values of the vertical load, in order to have an insight into the effects of a prestress on the overall flexural strength. The results are summarized in Fig. 12.20, where sections of the macroscopic yield surface are shown under biaxial bending (Fig. 12.20A) and horizontal bending and twisting (Fig. 12.20B), at increasing values of the vertical membrane stress N_{22}.

It is possible to notice that vertical membrane loads affect not only the horizontal bending moment, but also the vertical one, as bed joints are activated also when masonry is subjected to vertical bending moments.

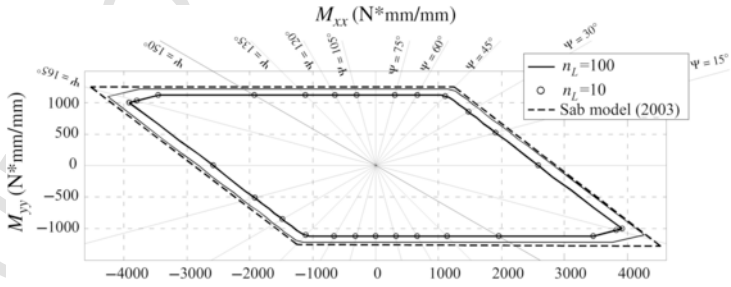

FIGURE 12.18 Yield surfaces in the (M_{xx},M_{yy})=(M_{11},M_{22}) plane obtained using the PES model with joints reduced to interfaces (number of layers n_L=10 or 100), and the Compatible Identification model (which coincides with Sab model in case of Kirchhoff-Love plates).

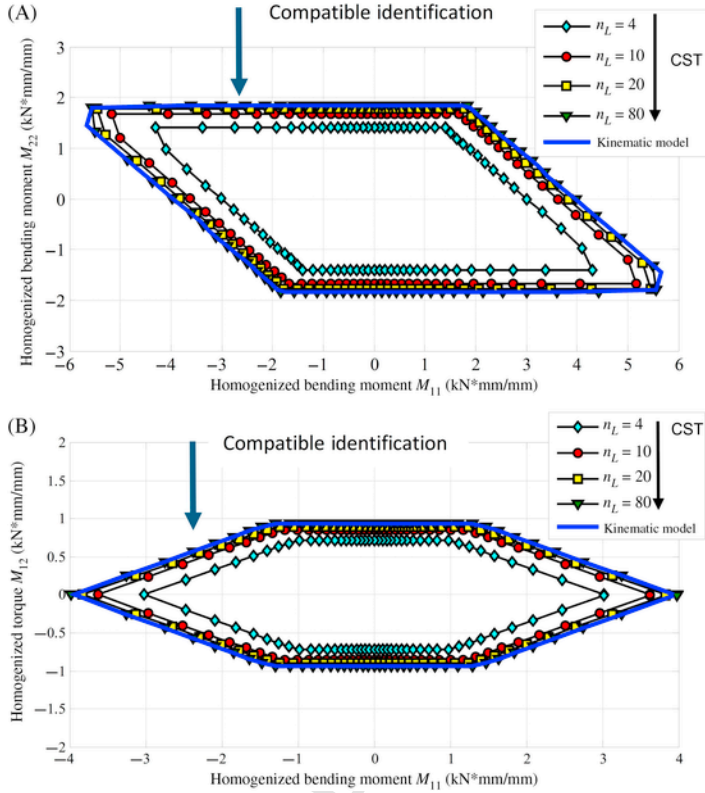

FIGURE 12.19 Yield surfaces obtained using the CST and compatible identification model by increasing the number of layers across the wall thickness. (A) Biaxial bending (M_{11},M_{22}); (B) horizontal bending and twisting (M_{11},M_{12}).

TABLE 12.2 Mechanical properties adopted for the out-of-plane numerical simulations in the presence of vertical precompression (standard Italian clay bricks).

Mortar joints reduced to interfaces (Mohr–Coulomb failure criterion with tension cutoff and linearized compressive cap)		
Cohesion (MPa)	c	$1.4\,f_t$
Tensile strength (MPa)	f_t	0.10
Compressive strength (MPa)	f_c	4.0
Friction angle (degree)	Φ	37
Shape of the linearized compressive cap (degree)	Φ_2	30

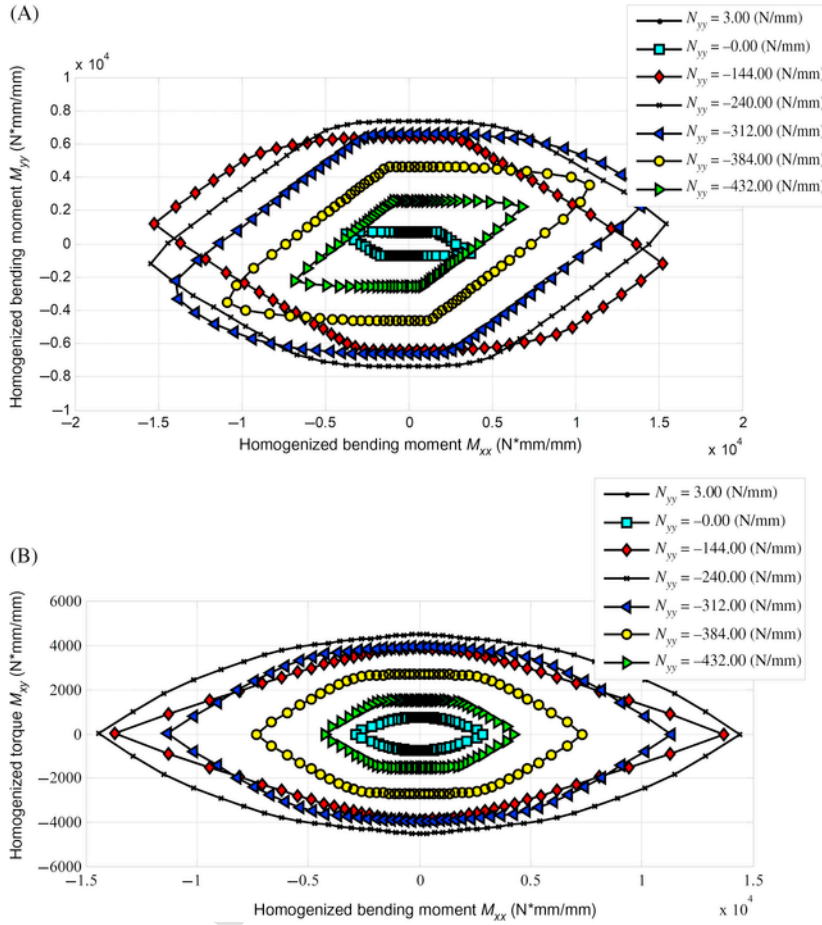

FIGURE 12.20 Yield surfaces obtained at increasing values of the vertical membrane stress, N_{yy}=N_{22} using the CST. (A) Sections in the plane (M_{11},M_{22})=(M_{xx},M_{yy}). (B) Sections in the plane (M_{11},M_{12})=(M_{xx},M_{xy}).

From Fig. 12.20 it can be observed that at high membrane stresses (around 0.7–0.8 times the compressive strength of the joints), a drop in the out-of-plane load bearing capacity of the wall occurs. In agreement with experimentation, it is possible to spot out an optimal compressive load at which the highest out-of-plane strength is attained. Beyond this optimum value, the out-of-plane strength starts to decrease until membrane crushing occurs. Obviously, a classic Mohr–Coulomb failure criterion is incapable of reproducing this important phenomenon, since failure in simple compression is not possible. In contrast, a model with limited compressive strength is able to better capture the behavior of masonry under combined in- and out-of-plane actions.

An interesting issue to discuss is the influence of the joint thickness on the out-of-plane homogenized failure surface. As already pointed out for the in-plane case, reducing joints to interfaces results in a slightly overestimated macroscopic strength. The MoC is a quite straightforward approach that allows the role played by the joint thickness to also be quantitatively evaluated for transversely loaded walls. In a further numerical example, the MoC is therefore utilized both assuming joints to be infinitely thin, or 10 mm-thick. A running bond wall built with common Italian clay bricks is considered, and the results obtained reducing joints to interfaces are compared with those derived accounting for the actual thickness. The possibility of failure in the units is discarded.

Two different failure surfaces are adopted for thick and thin joints, as shown in Fig. 12.21. Fig. 12.21A shows the plane stress multisurface failure criterion used for thick joints. The strength domain is obtained as the convex envelope of a Mohr–Coulomb failure criterion in plane strain conditions (characterized by a cohesion c and a friction angle Φ); a Rankine failure criterion in tension (characterized by a tensile strength f_t); and a linearized compression cap (characterized by three parameters, Φ_2, ρ, and f_c). The meaning of the symbols is explained in Fig. 12.21A. The second failure criterion applies to joints reduced to interfaces. In this case reference is made to the multilinear failure surface depicted in Fig. 12.21B, which is characterized by Mohr–Coulomb failure criterion, supplemented by a linear cap in compression (identified by two mechanical parameters, Φ_2 and f_c, defining the shape of the compression cap and the uniaxial compressive strength, respectively), and a tension cutoff (at a tensile strength equal to f_t). As can be noted from Fig. 12.21, the interface failure criterion is the exact counterpart of the 2D one used for thick joints, with a slight difference on the tension cutoff coming from the theoretical definition of the Rankine criterion.

The mechanical properties adopted for mortar are summarized in Table 12.3. Again, bricks are assumed to be infinitely resistant: this is a reasonable

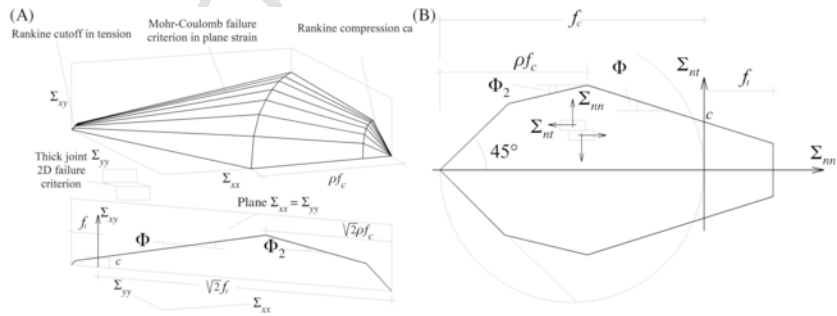

FIGURE 12.21 (A) Plane stress failure criterion adopted for thick mortar joints. (B) Interface failure criterion adopted for joints reduced to interfaces.

TABLE 12.3 Mechanical properties adopted for the out-of-plane numerical simulations (MoC model) without vertical precompression.

Mortar joints reduced to interfaces or with thickness equal to 10 mm (Mohr–Coulomb failure criterion with tension cutoff and linearized compressive cap)		
Cohesion (MPa)	c	$1.0\,f_t$
Tensile strength (MPa)	f_t	0.28
Compressive strength (MPa)	f_c	10.0
Friction angle (degree)	Φ	36
Shape of the linearized compressive cap (degree)	Φ_2	10
	ρ	0.5

assumption for clay brick masonry subjected to transverse loads, as failure is usually a consequence of the limited tensile and shear strength of the joints.

It is interesting to point out that the compressive strength assumed for mortar is sufficiently high to limit mortar crushing in the compressed fibers under bending. As a consequence, the homogenized out-of-plane strength basically depends only on the tensile and shear strength of mortar, so that the role of the joint thickness can be better understood.

In Fig. 12.22, three sections of the failure surface obtained with the MoC are represented, both for thin and thick joints. Subfigures (A)–(C) depict sections in the planes (M_{11},M_{22}), (M_{11},M_{12}), and (M_{22},M_{12}), respectively. A 3D representation of the whole failure surface in the (M_{11},M_{22},M_{12}) space is finally provided in Fig. 12.23: subfigure (A) refers to thin joints, whereas subfigure (B) refers to thick joints.

As can be noted, the failure surface obtained by the MoC closely matches that found by the Compatible Identification approach, as well as with the CST and PES lower bounds. The ultimate bending moment about the bed joints can be easily estimated by hand calculation as $M_{22}=f_t t^2/2$. Both in the presence of thin and thick joints, the prediction given by the MoC is in agreement with the theoretical value.

The same remarks apply to the ultimate twisting moment, which is simply given by $M_{12}=ct^2/4$. In the presence of joints reduced to interfaces, the analytical prediction is perfectly matched, whereas when the joint thickness is taken into account, a slight underestimation is observed. This can be explained remembering that the state of stress in thick bed and cross-joints is more complex than that in an interface.

The role played by the actual thickness of the joint is similar to that observed by Milani and Taliercio (2015) for the in-plane case and recalled in the previous section. Assuming comparable failure surfaces for thick and thin

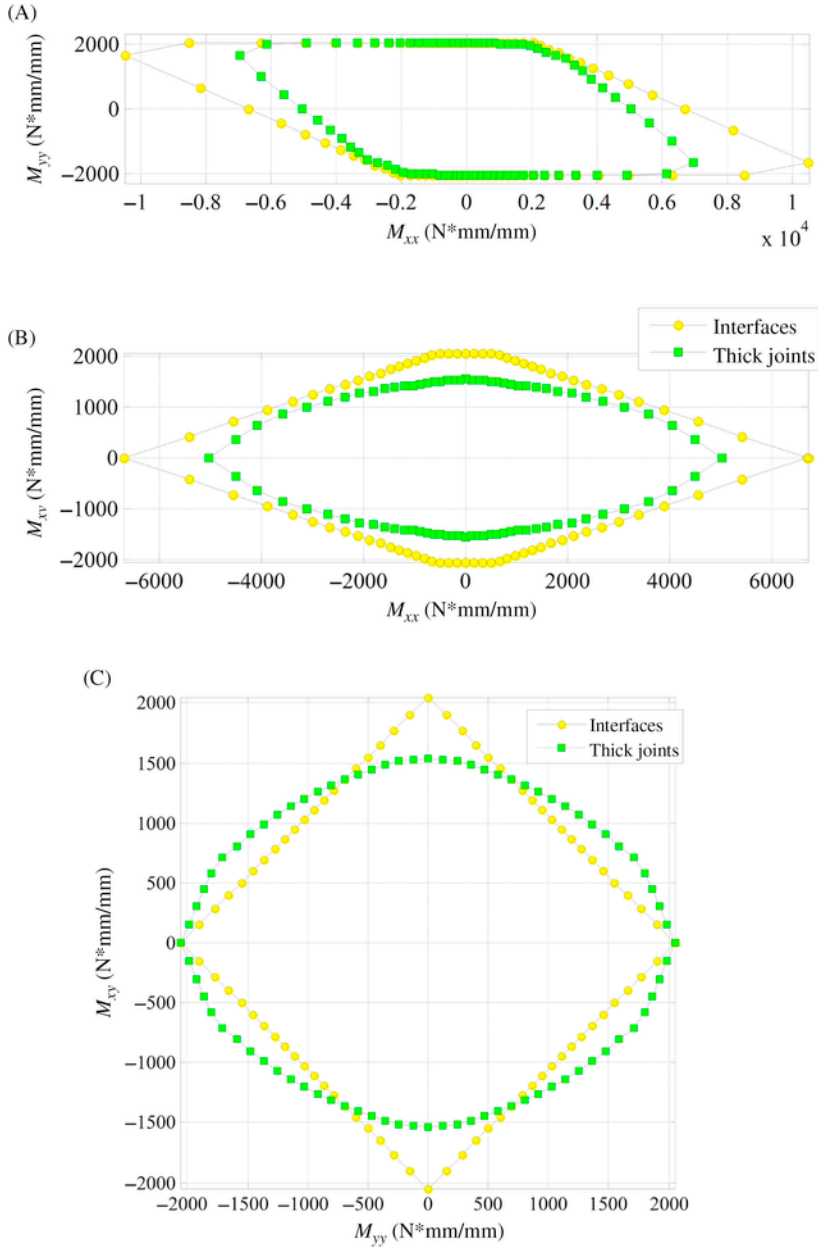

FIGURE 12.22 Sections of the failure surface obtained with the MoC model proposed in the planes of the macroscopic moments. (A) Plane $(M_{11},M_{22})=(M_{xx},M_{yy})$; (B) plane $(M_{11},M_{12})=(M_{xx},M_{xy})$; (C) plane $(M_{22},M_{12})=(M_{yy},M_{xy})$.

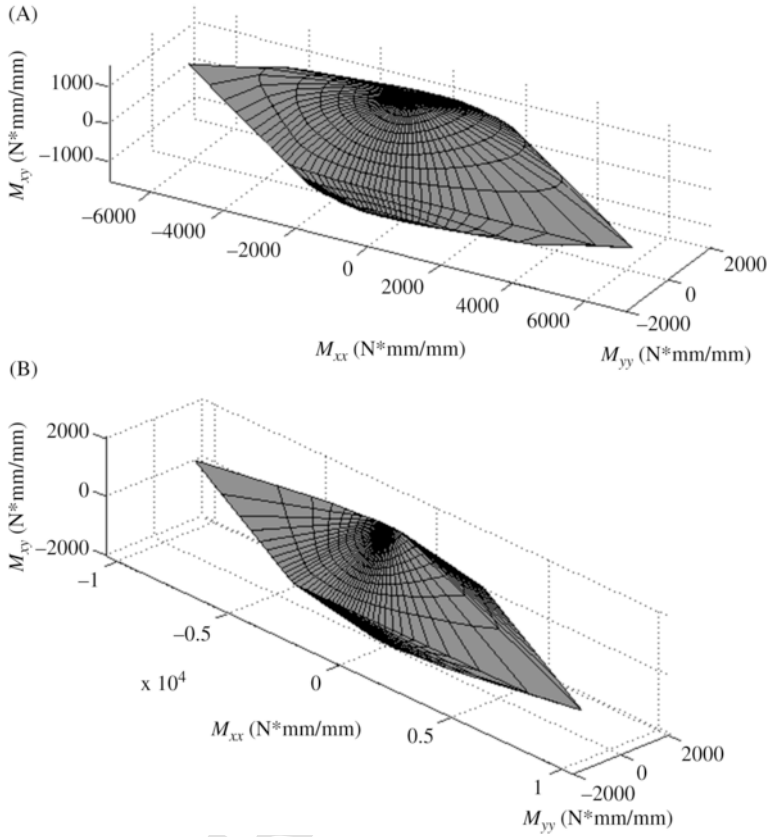

FIGURE 12.23 3D representation of the out-of-plane homogenized failure surfaces obtained by the MoC: (A) joints reduced to interfaces; (B) joint of finite thickness.

joints, a nonnegligible reduction in the out-of-plane homogenized strength is observed, especially in bending about the head joints (similar to what occurs for in-plane loads). As already pointed out for a twisting moment, this discrepancy is obviously a consequence of the complex state of stress in the bed joints under bending moment M_{11}, which cannot be effectively captured reducing joints to interfaces.

For some combinations of twisting (M_{12}) and bending moments about the bed joints (M_{22}), an extra strength is obtained taking the joint thickness into account (see Fig. 12.22C). This is likely to be a consequence of the different failure criteria adopted for thin and thick joints. Finally, note the apparent nonlinearity of the homogenized failure surface in the presence of thick joints (Fig. 12.23A) and the reduction to a multilinear yield surface when joints are reduced to interfaces (Fig. 12.23B).

12.9 CONCLUSIONS

Four simple homogenization models were proposed to derive homogenized strength domains for in- and out-of-plane loaded periodic brickwork. The first two procedures give lower bounds, whereas the last two approaches give upper bounds to the actual macroscopic strength domain.

In the first model, the elementary cell is subdivided into a few rectangular subdomains, where the microstress field is expanded using polynomial expressions. Four expansions were investigated in detail (P0, P2, P3, P4). P3 and P4 proved good convergence either to the actual solution in the case of joints reduced to interfaces, or to alternative upper bound approaches and FEM. Also, the second one yields a lower bound, where joints are reduced to interfaces and bricks are subdivided into a few CST elements. The third procedure is a kinematic compatible identification, which yields an upper bound to the macroscopic strength domain, where joints have been reduced to interfaces and bricks have been assumed to be infinitely resistant. The last model, MoC, is again a kinematic procedure where the elementary cell has been subdivided into six rectangular cells with preassigned polynomial periodic velocity fields. The first and latter models allow thick joint brickwork to be analyzed. A detailed comparison of the results provided by all models was given, both for under in-plane and out-of-plane loads, focusing in particular on the role played by the joint thickness.

All the proposed models give predictions that match available experimental results fairly well. Also, the numerical results obtained by the refined FE models can be reproduced at a much lower computational cost. In conclusion, the proposed models can be conveniently used to predict the loadbearing capacity of masonry structures. The choice of either one of the models depends on the joint thickness and the required degree of approximation.

REFERENCES

Aboudi, J., 1991. Mechanics of Composite Materials—A Unified Micromechanical Approach. Studies in Applied Mechanics, vol. 29, Elsevier, Amsterdam.

Anthoine, A., 1995. Derivation of the in-plane elastic characteristics of masonry through homogenization theory. Int. J. Solids Struct. 32 (2), 137–163.

Anthoine, A., 1997. Homogenization of periodic masonry: plane stress, generalized plane strain or 3D modelling?. Comm. Numer. Methods Eng. 13 (5), 319–326.

Berto, L., Saetta, A., Scotta, R., Vitaliani, R., 2002. An orthotropic damage model for masonry structures. Int. J. Numer. Methods Eng. 55, 127–157.

Cecchi, A., Milani, G., 2008. A kinematic FE limit analysis model for thick English bond masonry walls. Int. J. Solids Struct. 45 (5), 1302–1331.

Casolo, S., Milani, G., 2010. A simplified homogenization-discrete element model for the nonlinear static analysis of masonry walls out-of-plane loaded. Eng. Struct. 32 (8), 2352–2366.

Cecchi, A., Milani, G., Tralli, A., 2005. Validation of analytical multiparameter homogenization models for out-of-plane loaded masonry walls by means of the finite element method. J. Eng. Mech. ASCE 131 (2), 185–198.

Cecchi, A., Milani, G., Tralli, A., 2007. A Reissner-Mindlin limit analysis model for out-of-plane loaded running bond masonry walls. Int. J. Solids Struct. 44 (5), 1438–1460.

Cluni, F., Gusella, V., 2004. Homogenization of nonperiodic masonry structures. Int. J. Solids Struct. 41 (7), 1911–1923.

Dallot, J., Sab, K., Godet, O., 2008. Experimental validation of a homogenized plate model for the yield design of masonry wall. C. R. Mécanique 336, 487–492.

de Buhan, P., de Felice, G., 1997. A homogenisation approach to the ultimate strength of brick masonry. J. Mech. Phys. Solids 45 (7), 1085–1104.

de Felice, G., Giannini, R., 2001. Out-of-plane seismic resistance of masonry walls. J. Earthq. Eng. 5 (2), 253–271.

de Felice, G., 2011. Out-of-plane seismic capacity of masonry depending on wall section morphology. Int. J. Arch. Heritage 5 (4), 466–482.

Gazzola, E.A., Drysdale, R.G., Essawy, A.S., 1985. Bending of concrete masonry walls at different angles to the bed joints. In: Proc. 3th North. Amer. Mas. Conf., Arlington, TX, USA, paper 27.

Gilbert, M., Casapulla, C., Ahmed, H.M., 2006. Limit analysis of masonry block structures with nonassociative frictional joint using linear programming. Comput. Struct. 84, 873–887.

Kawa, M., Pietruszczak, S., Shieh-Beygi, B., 2008. Limit states for brick masonry based on homogenization approach. Int. J. Solids Struct. 45, 998–1016.

Lotfi, H.R., Shing, P.B., 1994. Interface model applied to fracture of masonry structures. J. Struct. Eng. ASCE 120 (1), 63–80.

Lourenço, P.B., 1996. Computational strategies for masonry structures. PhD thesis, TU Delft, The Netherlands.

Lourenço, P.B., 1997. An anisotropic macromodel for masonry plates and shells: implementation and validation. Report 03.21.1.3.07, University of Delft, Delft, Holland and University of Minho, Guimarães, Portugal.

Lourenço, P.B., Rots, J., 1997. A multisurface interface model for the analysis of masonry structures. ASCE J. Eng. Mech. 123 (7), 660–668.

Luciano, R., Sacco, E., 1997. Homogenisation technique and damage model for old masonry material. Int. J. Solids Struct. 34 (24), 3191–3208.

Lourenço, P.B., de Borst, R., Rots, J.G., 1997. A plane stress softening plasticity model for orthotropic materials. Int. J. Numer. Methods Eng. 40, 4033–4057.

Luciano, R., Sacco, E., 1998. Damage of masonry panels reinforced by FRP sheets. Int. J. Solids Struct. 35 (15), 1723–1741.

Macorini, L., Izzuddin, B.A., 2011. A nonlinear interface element for 3D mesoscale analysis of brick-masonry structures. Int. J. Numer. Methods Eng. 85, 1584–1608.

Milani, G., 2008. 3D upper bound limit analysis of multileaf masonry walls. Int. J. Mech. Sci. 50 (4), 817–836.

Milani, G., 2009. Homogenized limit analysis of FRP-reinforced masonry walls out-of-plane loaded. Comput. Mech. 43, 617–639.

Milani, G., 2011. Simple lower bound limit analysis homogenization model for in- and out-of-plane loaded masonry walls. Constr. Build. Mater. 25, 4426–4443.

Milani, G., 2011. Kinematic FE limit analysis homogenization model for masonry walls reinforced with continuous FRP grids. Int. J. Solids Struct. 482012, 326–345.

Milani, G., 2011. Simple homogenization model for the nonlinear analysis of in-plane loaded masonry walls. Comput. Struct. 89 (17-18), 1586–1601.
Milani, G., 2015. Upper bound sequential linear programming mesh adaptation scheme for collapse analysis of masonry vaults. Adv. Eng. Softw. 79, 91–110.
Milani, G., Tralli, A., 2011. Simple SQP approach for out-of-plane loaded homogenized brickwork panels accounting for softening. Comp. Struct. 89 (1-2), 201–215.
Milani, G., Taliercio, A., 2015. In-plane failure surfaces for masonry with joints of finite thickness estimated by a method of cells-type approach. Comput. Struct. 150, 34–51.
Milani, G., Taliercio, A., 2016. Limit analysis of transversally loaded masonry walls using an innovative macroscopic strength criterion. Int. J. Solids Struct. 81, 274–293.
Milani, G., Lourenço, P.B., Tralli, A., 2006. Homogenization approach for the limit analysis of out-of-plane loaded masonry walls. J. Struct. Eng. ASCE 132 (10), 1650–1663.
Milani, G., Lourenço, P.B., Tralli, A., 2006. Homogenised limit analysis of masonry walls. Part I: failure surfaces. Comput. Struct. 84 (3-4), 166–180.
Milani, G., Lourenço, P.B., Tralli, A., 2006. Homogenised limit analysis of masonry walls. Part II: structural examples. Comput. Struct. 84 (3-4), 181–195.
Minga, E., Macorini, L., Izzuddin, B.A., 2018. Enhanced mesoscale partitioned modeling of heterogeneous masonry structures. Int. J. Numer. Methods Eng. 113 (13), 1950–1971.
Minga, E., Macorini, L., Izzuddin, B.A., 2018. A 3D mesoscale damage-plasticity approach for masonry structures under cyclic loading. Meccanica 53 (7), 1591–1611.
Mistler, M., Anthoine, A., Butenweg, C., 2007. In-plane and out-of-plane homogenisation of masonry. Comput. Struct. 85, 1321–1330.
Pande, G.N., Liang, J.X., Middleton, J., 1989. Equivalent elastic moduli for brick masonry. Comput. Geotech. 8, 243–265.
Pegon, P., Anthoine, A., 1997. Numerical strategies for solving continuum damage problems with softening: application to the homogenisation of masonry. Comput. Struct. 64 (1-4), 623–642.
Pelà, L., Cervera, M., Roca, P., 2011. Continuum damage model for orthotropic materials: application to masonry. Comp. Methods Appl. Mech. Eng. 200, 917–930.
Pelà, L., Cervera, M., Roca, P., 2013. An orthotropic damage model for the analysis of masonry structures. Constr. Build. Mater 41, 957–967.
Pietruszczak, S., Niu, X., 1992. A mathematical description of macroscopic behavior of brick masonry. Int. J. Solids Struct. 29 (5), 531–546.
Portioli, F., Casapulla, C., Cascini, L., D'Aniello, M., Landolfo, R., 2013. Limit analysis by linear programming of 3D masonry structures with associative friction laws and torsion interaction effects. Arch. Appl. Mech. 83, 1415–1438.
Sab, K., 2003. Yield design of thin periodic plates by a homogenization technique and an application to masonry walls. C. R. Mécanique 331, 641–646.
Sab, K., Dallot, J., Cecchi, A., 2007. Determination of the overall yield strength domain of out-of-plane loaded brick masonry. Int. J. Multiscale Comput. Eng. 5 (2), 83–92.
Sacco, E., 2009. A nonlinear homogenization procedure for periodic masonry. Eur. J. Mech. A/Solids 28 (2), 209–222.
Shieh-Beygi, B., Pietruszczak, S., 2008. Numerical analysis of structural masonry: mesoscale approach. Comput. Struct. 86 (21-22), 1958–1973.
Stefanou, I., Sab, K., Heck, J.-V., 2015. Three dimensional homogenization of masonry structures with building blocks of finite strength: a closed form strength domain. Int. J. Solids Struct. 54, 258–270.
Suquet, P., 1983. Analyse limite et homogénéisation. C.R. Acad. Sci. Série IIB Mécanique 296, 1355–1358.

Suquet, P., 1987. Elements of homogenization for inelastic solid mechanics. In: Sanchez-Palencia, E., Zaoui, A. (Eds.), Homogenization Techniques for Composite Media. Springer, New York.

Sutcliffe, D.J., Yu, H.S., Page, A.W., 2001. Lower bound limit analysis of unreinforced masonry shear walls. Comput. Struct. 79, 1295–1312.

Taliercio, A., 2014. Closed-form expressions for the macroscopic in-plane elastic and creep coefficients of brick masonry. Int. J. Solids Struct. 51 (17), 2949–2963.

Taliercio, A., 2016. Closed-form expressions for the macroscopic flexural rigidity coefficients of periodic brickwork. Mech. Res. Commun. 72, 24–32.

Ushaksaraei, R., Pietruszczak, S., 2002. Failure criterion for structural masonry based on critical plane approach. ASCE J. Eng. Mech. 128 (7), 769–779.

Zucchini, A., Lourenço, P.B., 2002. A micromechanical model for the homogenization of masonry. Int. J. Solids Struct. 39 (12), 3233–3255.

Zucchini, A., Lourenço, P.B., 2007. Mechanics of masonry in compression: results from a homogenization approach. Comput. Struct. 85, 193–204.